BASIC RESEARCH ON CERAMIC MATERIALS FOR ENERGY STORAGE AND CONVERSION SYSTEMS

Progress Report

by

Donald H. Whitmore
Northwestern University
Evanston, Illinois 60201

December 1, 1979 to November 30, 1980

December 1980

Prepared for

THE U.S. DEPARTMENT OF ENERGY
Under Contract DE-AS02-76ERO 2564.A000

DISCLAIMER

Progress Report

covering the period from
December 1, 1979 to November 30, 1980

on

Contract DE-AS02-76ER02564.A000

Basic Research on Ceramic Materials for Energy
Storage and Conversion Systems

Abstract

The present research program involves utilizing appropriate experimental probes for measuring the movement of ionic and electronic charge carriers in ceramic materials suitable for solid electrolyte and electrode applications in high-performance, secondary battery and fuel cell systems. Special emphasis is placed on developing: (1) a better understanding of the effects of structure, impurities and composition on charge carrier transport mechanisms in such materials; and (2) detailed knowledge of the kinetics and mechanism of reactions occurring (on a microscopic scale) at the electrode-electrolyte interfaces of energy storage and conversion systems.

Notice

1. Enhancement of Ionic Transport in a Solid Electrolyte Containing a Finely Dispersed Inert Second-Phase

Personnel: J. B. Phipps, Ph.D. Candidate

1.1 Introduction

In an earlier phase of this research[1], it was found that microstructural refinement due to the addition of finely dispersed silica particles into a lithium iodide matrix could account for the two orders of magnitude increase in ionic conductivity first observed by Liang.[2,3] Three types of microstructural refinement occur when such inert particles are dispersed in lithium iodide: (1) interfaces are formed between the particles and the LiI matrix, (2) the grain boundary area is increased, (3) dislocations loops are created in the response to the stress generated at the particle/matrix interfaces due to differences in the thermal contraction coefficients of silica and lithium iodide.

It has been demonstrated that grain boundaries, surfaces, and dislocations can act as regions of fast ionic transport in alkali and silver halides as well as in semiconductors, metals, and oxides. The enhanced ion transport is a result of the structural disorder and the space-charge cloud associated with these features.[4]

The relationship between dislocation density and ionic conductivity of lithium iodide was studied by using two different types of silica (amorphous silica and cristobalite) as the inert particle additive. The thermal expansion coefficient of cristobalite more closely matches that of lithium iodide than does the coefficient for amorphous silica. As a result, we expect that a LiI/cristobalite composite would contain far less dislocations after a thermal cycle and, hence, have a lower ionic conductivity than would a LiI/amorphous silica composite.

The connection between the dislocation density and the conductivity was also demonstrated in our laboratory by quenching LiI/SiO_2 composites to various temperatures. For example, a composite quenched to $-185^{\circ}C$ exhibited a conductivity twice as large as the same sample showed when it was quenched to $20^{\circ}C$, which is a reflection of the larger dislocation density created in the composite quenched to the lower temperature ($-185^{\circ}C$).

It was first shown in our laboratory that the maximum enhancement of the conductivity of LiI/SiO_2 composites occurred at the isoelectric temperature, that is, at that temperature where the dislocations (as well as other vacancy sources and sinks) were uncharged (electrically neutral). At temperatures other than the isoelectric temperature, the dislocations possess a charge and this requires that an additional coulombic term must be added to the activation energy for vacancy motion.[5] When dislocations are uncharged at the isoelectric temperature, however, there is no coulombic interaction between the dislocations and the vacancies. Figure 1 dramatically illustrates the influence that the electric charge on the dislocations has on the ionic conductivity of the composite electrolyte.

The first phase of this study also indicated that microstructural refinement can substantially increase the ionic conductivity of lithium iodide. Others[6,7] have suggested that water may play an important role in the enhancement of ionic conductivity in lithium iodide. Owens[6] has proposed that water present on the surface of the additive particles (Al_2O_3 or SiO_2) reacts with lithium iodide to form the compound lithium iodide monohydrate. The monohydrate has an ionic conductivity of about $1 \times 10^{-5} (\Omega cm)^{-1}$ at 30°C compared with $2 \times 10^{-7} (\Omega cm)^{-1}$ for the fully dehydrated lithium iodide. A mixture of lithium iodide and $LiI \cdot H_2O$ should, therefore, possess a higher ionic conductivity than pure lithium iodide.

To assess the role that moisture plays in the conduction process, the second phase of our investigation focused on the $LiI-H_2O$ system by investigating the $LiI-H_2O$ phase diagram and the ionic conductivity/composition relationships in this system.

1.2 Experimental Procedure

The apparatus shown in Fig. 2 was used to measure the conductivity of $LiI \cdot x\ H_2O$ where $0 \leq x \leq 6$. This apparatus was also used to monitor the temperature of the samples as they were cooled from about 150°C to room temperature. The resulting "cooling curves" were used to generate the phase diagram shown in Fig. 3. Samples with different water contents were prepared by starting with the composition $LiI \cdot 6H_2O$ and evaporating under vacuum a specified amount of water to yield a new composition. This process was continued until the fully-dehydrated state was achieved.

Complex plane plots were obtained for the particular compositions with the aid of a vector impedance meter capable of scanning frequencies from 10 Hz to 500 kHz. An idealized impedance plot for $LiI \cdot xH_2O$ with platinum electrodes and the corresponding equivalent circuit is shown in Fig. 4. The low-frequency intercept with the real axis yields the bulk resistance.

A typical experiment would proceed as follows:

(1) vacuum evaporation of water at a sub-eutectic temperature;

(2) weighing the sample to determine its composition;

(3) heating sample to a temperature where it is completely liquid;

(4) slowly cooling the sample from that temperature while recording both the temperature and bulk resistance.

1.3 Results and Discussion

The $LiI-H_2O$ phase diagram was determined from cooling curves (temperature vs. time) and, in addition, the bulk resistance was monitored as each sample was cooled. From Fig. 5, it is evident that a strong correlation exists between the cooling curve and the resistance. To understand the specific nature of this correlation for the sample with composition $LiI \cdot 1.02\ H_2O$, it is first necessary to understand the processes which occurred as this sample was cooled. The particular processes can be deduced by consulting the $LiI-H_2O$ phase diagram (Fig. 3). Initially, the sample was in a liquid state at a temperature of about 160°C. The sample was then allowed to furnace cool. At about 131°C, the first solid phase (the monohydrate) appeared. Since solidification is an exothermic process, a change in slope was observed in the cooling curve at 131°C. Moreover, the resistance of the sample increased dramatically at 131°C due to a combination of effects. First, the resistance increased simply because a highly-conductive liquid was partially replaced by a much less-conductive solid phase. Second, as the sample cooled through the liquidus region the composition of the liquid phase became increasingly water-rich, that is, depleted in charge carrying Li^+ and I^- ions. This combination of effects resulted in a linear increase in the sample resistance with time (see Fig. 5) as cooling progressed through the liquidus region.

When the sample cooled to the eutectic temperature of 78.5°C, the small amount of liquid that still remained solidified,suddenly resulting in

a small exothermic plateau in the cooling curve and a large increase in the sample resistance. At temperatures less than 78.5°C, the resistance was characteristic of a solid composed of hydrate phases, $LiI \cdot H_2O$ and $LiI \cdot 2H_2O$.

The sample conductivity as a function of its water content at 28°C is plotted in Fig. 6. It is evident from this figure that the monohydrate is much more conductive than any other composition (by a factor of about sixty). The relationship between conductivity and composition can be clarified by consulting the $LiI-H_2O$ phase diagram. First, consider the compositional region extending from the monohydrate to the dihydrate. The phase diagram for this region has a simple eutectic at the composition $LiI \cdot 1.7\ H_2O$ and the temperature 78.5°C. The microstructure of a sample with a composition between $LiI \cdot H_2O$ and $LiI \cdot 1.7\ H_2O$ (hypoeutectic) will be different than the microstructure of compositions lying between $LiI \cdot 1.7\ H_2O$ and $LiI \cdot 2\ H_2O$ (hypereutectic). For hypereutectic compositions, the microstructure should consist of proeutectic dihydrate grains embedded in an interconnected matrix phase with the eutectic composition. The eutectic composition is a mixture of 30 mole percent monohydrate and 70 mole percent dihydrate. In contrast, a sample with a hypoeutectic composition should be composed of monohydrate grains embedded in the same eutectic matrix. The composition $LiI \cdot 1.7\ H_2O$, then, acts as the line of demarcation between two distinctly different microstructures. It is evident from Fig. 7 that the ionic conductivity of hydrated lithium iodide is dependent on microstructure. Note the distinct change in slope which occurs at the eutectic composition of $LiI \cdot 1.7\ H_2O$.

To this point, a qualitative relationship between ionic conductivity and microstructure has been established. A quantitative treatment requires that the microstructure for each composition be known. It has been hypothesized that the microstructure for compositions between the monohydrate and dihydrate consists of proeutectic grains embedded in a eutectic matrix. To a first approximation, then, the overall microstructure consists of spheres embedded in a continuous matrix phase. The relative amounts of proeutectic and eutectic phases may be readily determined by using the lever rule.

In 1881, J. C. Maxwell[8] derived several expressions relating conductivity to structure for a number of composites. One type of composite he

considered consisted of spheres, with volume fraction V_v and conductivity σ_s, embedded in a matrix of conductivity σ_m. The composite conductivity σ_c was determined by Maxwell to be

$$\sigma_c = \frac{2\sigma_m (1-V_v) + \sigma_s (1 + 2V_v)}{\sigma_m (2+ V_v) + \sigma_s (1 - V_v)} \sigma_m$$

Maxwell's theoretical composite conductivity as given by this last expression is compared with the conductivity data for compositions lying between $LiI \cdot H_2O$ and $LiI \cdot 1.7\ H_2O$ in Fig. 8. The fit between Maxwell's theory and the data is exceptionally good.

Also plotted in Fig. 8 is the conductivity to be expected if the microstructure shown in Fig. 9 was assumed to exist. The composite conductivity for such a microstructure is

$$\sigma_c = \tfrac{1}{4} \{(3x_2 - 1)\ \sigma_2 + (3x_1 - 1)\ \sigma_1 + [\ (3x_2 - 1)\ \sigma_2 + (3x_1 - 1)\ \sigma_1)^2 + 8\ \sigma_1\sigma_2]^{\frac{1}{2}}\}$$

Landauer[9] derived this last expression by assuming that each grain was surrounded by an "effective medium" of conductivity σ_c consisting of randomly distributed grains of two types with conductivities σ_1 and σ_2 and volume fractions x_1 and x_2.

It is clear from Fig. 8 that a microstructure composed of monohydrate spheres embedded in a continuous eutectic matrix more closely approximates the actual microstructure of our sample than does a microstructure composed of a random distribution of eutectic and monohydrate grains.

Let us now consider compositions in the range from LiI to $LiI \cdot H_2O$. In general, the conductivity increases rapidly as the water content increases. However, at about the composition $LiI \cdot \frac{1}{2}\ H_2O$, a plateau in the conductivity occurs as shown in Figs. 6 and 10. Figure 10 also compares the observed conductivity to Maxwell's theory and effective medium theory. In line with Maxwell's ideas, we assumed that we have proeutectic spheres of lithium iodide embedded in a continuous eutectic matrix with an overall composition of $LiI \cdot 0.9\ H_2O$. To test the effective medium theory, a random mixture of lithium iodide and eutectic grains was assumed.

While neither model exactly matches the observed data, it is apparent that closer agreement is achieved using the effective medium theory. Even better agreement between the effective medium theory and the data is achieved if a distinct phase (with an overall composition of $LiI \cdot \frac{1}{2} H_2O$) is assumed to exist (see Fig. 11). It should be noted, however, that cooling curve data provides no evidence for the existence of a phase with this composition. In addition, while Hüttig and Steudemann[10] report the existence of a eutectic at $LiI \cdot 0.9 H_2O$, neither the cooling curve data nor the conductivity data from this study indicated the existence of such a eutectic. Based on this study, peritectic solidification, rather than eutectic solidification at 131°C, seems more likely.

In summary, then, the dependence of conductivity on water content for compositions ranging from LiI to $LiI \cdot H_2O$ is very different than for compositions ranging from $LiI \cdot H_2O$ to $LiI \cdot 1.7 H_2O$. For the composition range $LiI \cdot H_2O$ to $LiI \cdot 1.7 H_2O$, the conductivity is indicative of a microstructure likely to result from eutectic solidification and in agreement with Maxwell's theory. For compositions ranging from LiI to $LiI \cdot H_2O$ the conductivity is more indicative of a microstructure which consists of distinct grains and these data show only marginal agreement with the predictions of the effective medium theory. This type of microstructure may be favored when peritectic solidification occurs. A more thorough investigation of the ionic conductivity for samples with compositions between LiI and $LiI \cdot H_2O$ is clearly needed and will be undertaken soon.

Since both temperature and resistance are monitored in our experiments, standard Arrhenius plots can be made for each composition. The Arrhenius plot for the composition $LiI \cdot 0.77 H_2O$ is compared to dehydrated lithium iodide in Fig. 12. The dehydrate shows two-slope behavior: the high temperature (intrinsic) region has a slope which is characteristic of the energies of vacancy formation and migration and the extrinsic low-temperature region has a slope which is proportional to the energy of ion migration alone. The Arrhenius plot for the composition $LiI \cdot 0.77 H_2O$ is very different. Here, a sharp change in conductivity occurs at the eutectic temperature of 131°C. Like the dehydrated lithium iodide, the composition of $LiI \cdot 0.77 H_2O$ also

exhibits a linear region at low temperatures. Figure 13 focuses on this low-temperature region for a number of compositions which fall between LiI and $LiI \cdot H_2O$. It is clear from this figure that the activation energy, as well as the pre-exponential factor, increases as the water content increases. Figures 14 and 15 compare the experimental activation energies and pre-exponential factors with those predicted by Maxwell's theory and the effective medium theory. It is evident from these figures that neither theory satisfactorily explains the experimental observations.

The work of D. K. Hohnke[11] on indium doped zirconia ($Zr_{1-x}In_{2x}O_{2-x}$) may provide still another explanation for the dependence of activation energy and pre-exponential factor on water content. He observed that a plot of the logarithm of the pre-exponential factor versus the activation energy for $Zr_{1-x}In_{2x}O_{2-x}$ gave a straight line, implying that the pre-exponential factor is exponentially related to the activation energy. Hohnke related this behavior to long-range ordering of oxygen vacancies in the electrolyte $Zr_{1-x}In_{2x}O_{2-x}$. A similar plot for $LiI \cdot xH_2O$ ($0 \leq x \leq 1$) is shown in Fig. 16. The linearity of this plot is striking and suggests that it may be possible to explain the relationship between conductivity and water content observed in our samples by a model based on vacancy ordering rather than microstructure. Figures 16 and 17 also compare the experimental data to Maxwell's theory and effective medium theory. While the effective medium theory approximates the linear behavior, more extensive research is needed before the nature of the dependence of conductivity on water content can be determined for $LiI \cdot xH_2O$ ($0 \leq x \leq 1$).

The first phase of this investigation concluded that microstructural refinement of lithium iodide via the addition of finely dispersed particles can greatly enhance the ionic conductivity. The second phase confirmed that the formation of the monohydrate phase can also substantially increase the ionic conductivity. Prior to this study, the most important factor contributing to the enhanced ionic conductivity in $LiI\text{-}Al_2O_3$ or $LiI\text{-}SiO_2$ composites was thought to be the formation of the monohydrate. However, microstructural refinement is more likely the cause of the enhanced ionic conductivity phenomenon first reported by Liang et.al.[2,3] for $LiI\text{-}Al_2O_3$ composites.

This conclusion is based on the information contained in Fig. 14. It is clear from this figure that even a small amount of water significantly increases the activation energy. Less than five mole percent water increases the activation energy by about twenty percent. In contrast, conductivity enhancement due to microstructural refinement does not affect the activation energy. Liang and associates reported that the ionic conducticity of lithium iodide was enhanced by a factor of 800 by the addition of Al_2O_3 particles. They also noted that the activation energy remained the same as that found for pure lithium iodide, that is, 0.4 eV. One is forced to conclude that the cause of the enhancement observed by Liang et. al. was not due to the formation of the monohydrate, as suggested by Owens and others, but is more likely a result of microstructural refinement.

2. Sodium Ion Transport in NASICON ($Na_3Zr_2Si_2PO_{12}$)

Personnel: Y.-T. Tsai and J. Dygas, Ph.D. Candidates

2.1 Introduction

NASICON has attracted a great deal of interest recently because of its potential as the solid electrolyte in sodium-sulfur batteries. The following important properties make NASICON a promising electrolyte for the sodium-sulfur cells:

(1) high Na^+ ion conductivity[12] ($0.4\ \Omega^{-1}cm^{-1}$ at 300^oC)and negligible electronic conductivity;

(2) three dimensional sodium conduction and nearly isotropic thermal expansion;[13]

(3) insensitivity to moisture and stability in molten sodium and sulfur;[14]

(4) easy fabrication into dense ceramic from inexpensive materials.

Hong[13] was first to synthesize this material and show that the system $Na_{1+x}Zr_2Si_xP_{3-x}O_{12}$ ($0 \leqslant x \leqslant 3$) has a skeleton or framework structure which consists of ZrO_6 octahedra corner-shared with SiO_4 and PO_4 tetrahedra with intersecting tunnels which form a three-dimensional network for rapid sodium ion transport. At room temperature, these compounds crystallize in the rhombohedral phase except for the highly-conducting compositions ($1.8 \leqslant x \leqslant 2.2$) which have monoclinic symmetry (space group C2/c).

Conductivity[12,15-20] and NMR[21] measurements have been reported for NASICON. NMR results show that spin-lattice relaxation time T_1 has different slopes in two different temperature regions corresponding to activation energies 0.13 eV above 227°C and 0.39 eV between 127° and 227°C.

Von Alpen at.al.[15] reported a second-order phase transition for NASICON from the monoclinic to a rhombohedral phase at about 147°C. However, transition temperatures different from that of von Alpen for this phase change have been reported recently by Boilot et.al.[16] and by Desplanches et.al.[17]

In the $(Zr_2Si_2PO_{12})^{3-}$ skeleton of the NASICON structure, each ZrO_6 octahedron shares its six corners with PO_4 and SiO_4 tetrahedra. Each of these tetrahedra, in turn, shares its four corners with ZrO_6 octahedra. In the monoclinic phase, three non-equivalent sodium sites, the M_1, M_2 and M_3 sites, are connected three-dimensionally such that each M_1 site is connected by two M_2 sites and four M_3 sites, and each M_2 or M_3 site is linked to two M_1 sites. All the M_1 and M_2 sites are occupied, while only one-half of the M_3 sites are occupied.

One method for fabricating NASICON involves the following procedures:[22] mechanical mixing of proper amount of Na_2CO_3, ZrO_2, SiO_2 and $NH_4H_2PO_4$, calcination at 1160°C, dry or wet ball milling, isostatic pressing, and sintering at 1230° to 1260°C for 4-24 hours. Traces of free zirconia were observed in the sintered bodies. Gordon et al.[22] obtained very dense (> 99% theoretical density) samples of NASICON by hot-pressing the calcined powder mixture (mechanically mixed) in a graphite die at temperatures between 1160° and 1240°C at pressures around 34 MPa.

Boilot et.al.[16] developed a chemical process for the preparation of NASICON. This involves the formation of a solid gel from three saturated water solutions of sodium silicate, $(NH_4)_2\ HPO_4$, and $ZrO(NO_3)_2 \cdot 2H_2O$. The calcined powder prepared from this process could be sintered at 1250°C to about 90% of theoretical density.

2.2 Synthesis of Polycrystalline NASICON and Conductivity Measurements at Low Frequencies

Dense (> 97% theoretical density) polycrystalline samples of NASICON

were prepared in our laboratory by the following procedures:

(1) vibratory milling of the proper amount of Na_2CO_3, ZrO_2, SiO_2 and $NH_4H_2PO_4$ with heptane;

(2) calcination of the dry milled powder at 1150°for 16 hours;

(3) vibratory milling of the calcined powder with heptane;

(4) isostatic pressing of the dry powder to 55,000 psi with PVB as a binder;

(5) sintering of the pressed pellets in air at 1250°C for 8 hours.

The density of each sample was measured by weighing the sample before, during and after immersion in a non-reactive solvent such as heptane. X-ray diffraction patterns were obtained with a diffractometer using copper K_α Ni-filtered radiation. The patterns obtained agreed with the calculated pattern[15] based on the monoclinic symmetry. Traces of free zirconia were observed in these samples.

The electrical conductivity of NASICON was measured as a function of temperature from 25° to 350°C using both blocking and reversible electrodes in a dry nitrogen atmosphere. At each temperature, data were collected with the computer-monitored automatic analyzer system in our laboratory or with the HP 4800A vector impedance meter. Corrections for the inductance of the measuring lead wires were made. These data were analyzed using complex plane plots and the nonlinear least-squares data-fitting program described later in this Report.

Schematic diagrams for the measuring cell with reversible electrodes and the corresponding equivalent circuits are shown in Figures 18 to 21. Typical complex admittance plots are shown in Figures 22 and 23. Figures 24 and 25 show the equivalent circuits and typical complex admittance plots for the case of using blocking electrodes.

From these observations, it has been possible to separate bulk conductivity from that of the grain boundaries. An Arrhenius plot ($\ell n\, \sigma T$ versus 1/T) shows two distinct slopes for the bulk which undergoes a phase transition between 120° and 200°C. The enthalpies of the bulk Na^+ ion motion are 0.19 to 0.21 eV for the high-temperature phase and 0.34 to 0.36 eV for the low-temperature phase. Arrhenius plots for bulk and grain boundaries are shown in Fig. 26. A comparison of the results of present work with those of

von Alpen et al.,[15] Boilot et al.,[16] and Hooper[20] is shown in Fig. 27.

2.3 Measurements of the Conductivity and Dielectric Constant at Microwave Frequencies

The ionic conductivity of NASICON was initially measured in our laboratory at low frequencies (< 500 kHz) and then at the microwave frequency of 24 GHz, both sets of measurements being made over the temperature range from 20° to 450°C. The complex impedance of a NASICON sample (94.5% of the theoretical density) was measured over frequency range from 5 Hz to 500 kHz using a vector impedance meter. The ionic conductivity of the bulk material was extracted from these data by analyzing the complex admittance plots at several temperatures within the foregoing range. The Arrhenius plot of conductivity was not linear over the entire range: there was a change of slope experienced at a temperature of approximately 200°C. For the low-frequency data in the temperature range from 20° to 180°C, one infers that the apparent activation energy ΔE_a was $\Delta E_a \approx 0.41$ eV, whereas, in the temperature region from 220° to 450°C, $\Delta E_a \approx 0.15$ eV.

After a set of measurements which involved maintaining the sample in a dry nitrogen atmosphere at about 400°C for several hours, black spots were apparent on the surface of the sample. These were ascribed by us to a partial reduction of the sample by its reaction with the ambient gas atmosphere. The influence of surface reduction on conductivity was investigated by temperature cycling the sample in air and in dry nitrogen. Reduction was partly reversible and change of sample impedance spectrum was observed. Definite conclusions concerning these observations require further analytical treatment of the data.

Under development in our laboratory is a computer program which will utilize nonlinear regression routines (with unequal weighting factors) to fit parameters of the equivalent circuit or of phenomenological expressions which describe the low-frequency impedance (or admittance) spectra of ionically-conducting samples. Such a program should enable us to make more accurate analyses of the experimental data and hence a critical comparison of different hypotheses which might be proposed to explain the spectra.

For measurements of σ and ϵ' at 24 GHz, parallelipiped samples were cut to fit into a rectangular waveguide from the same pellet which had been used for the aforementioned impedance measurements. Several difficulties

were encountered in employing the short-circuit line method with a stainless steel pressurized waveguide at temperatures up to 450°C. Choosing an appropriate length for our fairly conductive NASICON sample and applying accurate corrections for thermal expansion of the waveguide were found to be crucial if one is to obtain acceptable precision for the conductivity and dielectric constant values observed at 24 GHz.

A computer program was developed to compute both the conductivity and dielectric constant, as well as their limits of uncertainty, from standing-wave pattern observed in experiment. Analytical calculations were made of errors in the short-circuit line method as a function of sample thickness, assuming several values of conductivity and dielectric constant. The influence of each of the different sources of experimental error was assessed on the final precision of the σ and $\bar{\epsilon}$ values, with a view to designing our experiments so as to obtain the greatest precision from the observations. Application of a variable short-circuit line method appears to be a desirable direction for future measurements.

The Arrhenius plot of the best conductivity data observed to date at 24 GHz is nonlinear and shows an approximate two-slope behavior, with the change of slope occurring around 200°C, as was the case with the low-frequency conductivity data. The apparent activation energies are distinctly different, however, from those found in our low frequency measurements, being $\approx$ 0.15 eV in the high-temperature region and $\approx$ 0.18 eV in the low-temperature region. The microwave conductivity at 350°C was higher by a factor of 1.5 than that found at the lower frequencies for the bulk material at the same temperature. Further measurements will be necessary to confirm these preliminary results. New samples of polycrystalline NASICON will be prepared in the usual way and the σ and $\bar{\epsilon}$ measurements will be repeated at the microwave frequency of 24 GHz, as well as at several other frequency bands 10, 40, 70 and 130 GHz These observations should provide a good basis for understanding the dynamic behavior of sodium ions in the framework structure of NASICON.

3. A New and Improved Method for the Analysis of Complex Impedance (Admittance) Data

Personnel: Y.-T. Tsai, Ph.D. Candidate

The observed complex admittance (or impedance) plots usually consist of depressed semicircles and inclined straight lines. In most cases, the semicircles and straight lines are sufficiently separated on a complex-plane plot to allow the determination of the useful circuit parameters with the aid of a compass. However, results in our laboratory have often shown complex plane plots exhibiting overlapping semicircles and straight lines, indicative of phenomena with comparable relaxation frequencies. Accordingly, we felt that there was an obvious need to apply non-linear curve-fitting routines so that one could obtain reliable and accurate determinations of the individual circuit parameters in these latter structures.

The procedures developed in our laboratory for analyzing a complex-impedance diagram, consisting of two semicircles, will be discussed here. These procedures can also be used in analyzing complex-admittance diagrams. Application to the systems with more than two semicircles or combinations of semicircles and straight lines is also possible by incorporating separate subroutines for the individual components.

The empirical formula which describes a single semicircle in the complex impedance plot[23] is:

$$Z(\omega) = Z_{m-1} + \frac{Z_m - Z_{m-1}}{1 + \left(i \frac{\omega}{\omega_{o,m}}\right)^{1-\alpha_m}} \qquad (1)$$

where

$Z(\omega)$ = complex impedance at angular frequency ω

Z_{m-1} = high-frequency real intercept of $Z(\omega)$

Z_m = low-frequency real intercept of $Z(\omega)$

$\omega_{o,m}$ = relaxation frequency

α_m = depression parameter

The total impedance is the vector sum of two individual semicircles.

Rearranging Eq. (1), one obtains

$$\ell n \left| \frac{Z_m - Z(\omega)}{Z(\omega) - Z_{m-1}} \right| = (1 - \alpha_m) \ell n\, \omega - (1 - \alpha_m) \ell n\, \omega_{o,m} \qquad (2)$$

From Eq. (2) it is seen that a plot of $\ell n \left| \frac{Z_m - Z(\omega)}{Z(\omega) - Z_{m-1}} \right|$ vs. $\ell n\, \omega$ should yield a straight line with a slope of $(1 - \alpha_m)$. The extrapolation of this straight line to the frequency axis gives $\ell n\, \omega_{o,m}$. With the estimated values of Z_m, Z_{m-1}, $\omega_{o,m}$, and α_m, one can then calculate the approximate values at all measured frequencies.

The following procedures, similar to those described by Kleitz and Kennedy[23], are used to resolve two semicircles in the complex impedance plots:

(1) select a portion of the experimental data set with a minimum of overlapping;

(2) estimate the average position for the center of the circle and the values of the parameters Z_{m-1}, Z_m, and α_m, (the depressed angle is given by $\frac{\alpha_m \pi}{2}$);

(3) refine these parameters using a non-linear least-squares program developed by Marquardt (available from IBM share library distribution No. 309401, 1966). [Based on Marquardt's program, we have written a program for this study in Fortran II Code. The validity of this modified program has been tested against a sample data set of the original program with the accuracy to the sixth digit after decimal point];

(4) determine the distribution of the depression parameter $\alpha_{d,m}$ and the relaxation frequency $\omega_{o,m}$ using Eq. (2);

(5) calculate the theoretical impedance at all measured frequencies using Z_{m-1}, Z_m, $\omega_{o,m}$ and $\alpha_{d,m}$ determined from steps (3) and (4);

(6) calculate the differences between the experimental data and those of the approximated values obtained in step (5);

(7) approximate the second semicircle from this difference following steps (1) to (5);

(8) iterate procedures (1) to (7) until the preset criteria have been met. (The most convenient criterion is the average difference between the approximated and the experimental results after step (7). The convergence of intermediate resistance value Z_m can be used as another criterion)

This computer program has been proved useful in resolving two overlapping semicircles provided that the data points cover a reasonably wide range over the extreme zones where the overlapping is small.

Further improvement can be made by considering the complex impedance as a multiple dependent variable with the angular frequency as the independent variable. In this instance, the expression for $Z(\omega)$ is given by:

$$Z(\omega) = Z_{m-1} + \frac{Z_m - Z_{m-1}}{C}\left[1 + \left(\frac{\omega}{\omega_{o,m}}\right)^{1-\alpha_m} \cos \tfrac{1}{2}(1-\alpha_m)\pi\right] - i\,\frac{Z_m - Z_{m-1}}{C}\left[\left(\frac{\omega}{\omega_{o,m}}\right)^{1-\alpha_m} \sin \tfrac{1}{2}(1-\alpha_m)\pi\right] \qquad (3)$$

where

$$C = \left[1 + \left(\frac{\omega}{\omega_{o,m}}\right)^{1-\alpha_m} \cos \tfrac{1}{2}(1-\alpha_m)\pi\right]^2 + \left[\left(\frac{\omega}{\omega_{o,m}}\right)^{1-\alpha_m} \sin \tfrac{1}{2}(1-\alpha_m)\pi\right]^2$$

Here we have a problem of refining eight parameters $Z_{m-1}^{(1)}$, $Z_m^{(1)}$, $\omega_{o,m}^{(1)}$, $\alpha_m^{(1)}$, $Z_{m-1}^{(2)}$, $Z_m^{(2)}$, $\omega_{o,m}^{(2)}$, $\alpha_m^{(2)}$ with a single imdependent variable ω. A nonlinear, least-squares curve-fitting program can be constructed to adjust these parameters by minimizing the variance between the experimental and the calculated values.

4. Fast Protonic Conductors

Personnel: Y.-T. Tsai, Ph.D. Candidate

4.1 Introduction

A few months ago, we initiated a research effort on ion conduction mechanisms in solid electrolytes exhibiting high protonic conduction. This effort was nucleated as a result of the recently reported work of Farrington and Briant[24,25] in which it was demonstrated that the entire sodium ion content of β''-alumina could be exchanged for H^+, $H(H_2O)_x^+$ and NH_4^+ ions. All of the resulting compounds are protonic conductors exhibiting conductivities which vary with composition. The highest conductivity reported for this class of materials is 10^{-4} $(\Omega\ cm)^{-1}$ at 25°C for the ammonium-hydronium β''-alumina (typically $(NH_4)_{1.00}\ (H_3O)_{0.67}\ Mg_{0.67}\ Al_{10.33}\ O_{17}$).

An interconnected H_2O - H_3O^+ column oxygen network, which can form in the β″-structure was suggested by Farrington and Briant as the fast proton conduction path. However, the detailed atomistic transport mechanism(s) of protons in these materials is far from being understood and undoubtedly will involve some cooperative transport mechanisms. Our research program on protonic conductors is designed, then, to further our understanding of the protonic conduction processes occurring in such solid materials as β″-alumina and gallate and will stress the use of experimental probes such as pulsed, field-gradient NMR, optical spectroscopy and dielectric relaxation to accomplish this end. Details of our proposed research plan for this part of our program will be found in our 1980 Proposal to DOE.

4.2 Preliminary Experiments

Protonic β″-gallate single crystals have been prepared in our laboratory by immersing crystals[26] of sodium β″-gallate in molten ammonium nitrate for 14 days, followed by washing with anhydrous methanol and drying in air. The sodium content of the nitrate bath was determined by a flame spectroscopic method and the gallate crystal was also weighed before and after the exchange process. Preliminary conductivity measurements were carried out in a dry nitrogen atmosphere on a small single crystal sample (1 x 1.5 x 0.07 mm) with sputtered gold electrodes. Conductivity was measured as a function of temperature as shown in Fig. 28. For the temperature range 25° to 120°C, an activation energy for protonic motion of 0.40 eV was calculated from the data shown in Fig. 28.

Figure 29 shows a room temperature Raman spectrum of this material[27] between 80 cm^{-1} and 300 cm^{-1} with the laser beam parallel to the c-axis of the single crystal. Several distinct peaks were found between 80 cm^{-1} and 200 cm^{-1}. The results of this Raman work are still being analyzed.

5. Polymer Electrolytes Exhibiting Fast Alkali Ion Conduction

Personnel: R. Dupon and Y.-T. Tsai, Ph.D. Candidates.

5.1 Introduction

Current interest in the development of high energy-density batteries has focused considerable attention on solid electrolytes. The leading solid electrolytes in developmental batteries are hard ceramic materials, which usually are employed at elevated temperatures with liquid electrodes. A

more compliant solid electrolyte, such as a polymer electrolyte, should enable contact to be maintained at the electrode-electrolyte interfaces in an all solid state battery and lower operating temperatures might be facilitated. Complexes of poly(ethylene oxide)(PEO) or poly(propylene oxide)(PPO) with various alkali metal salts have been shown by Armand[1,2] to exhibit ionic conductivities which exceed $10^{-5}(\Omega\ cm)^{-1}$ at moderate temperatures.[28,29] The original synthesis and characterization of these materials was reported by Wright[30,31] and extended by James et al.[32]

5.2 Preliminary Experiments

A fundamental parameter in the characterization of any solid electrolytes is the fraction of the total current which is carried by the mobile ion, i.e., the transference number. Prior to the present work, a rigorous determination of the transference number of poly(ethylene oxide)-based electrolytes was not available. The present study is based on the measurement of emf between ion reversible amalgam electrodes which are separated by the solid electrolyte in a concentration cell.[33]

Poly(ethylene oxide) with an average molecular weight 600,000 was obtained from Aldrich. The polymer was purified by ion-exchange of an aqueous solution and the solvent was subsequently removed under high vacuum. Reagent grade NaSCN was recrystallized from methanol and dried under high vacuum. Reagent grade methanol was dried by distillation from iodine-activated magnesium under a nitrogen atmosphere.

A PEO·NaSCN complex, 4.5:1 mole ratio of polymer repeat unit to salt, was prepared from stoichiometric quantities of the polymer and salt in anhydrous methanol. Following complete dissolution of the two solids, the methanol was removed under vacuum. All manipulations were carried out using standard inert atmosphere techniques.[34] The identity of the PEO·NaSCN complex was confirmed by infrared spectroscopy and differential scanning calorimetry, and in previous research the material prepared by this same procedure has been characterized by optical microscopy and x-ray diffraction which demonstrate the absence of free NaSCN.

Amalgams were prepared with triple distilled mercury and reagent grade sodium. Molten sodium was filtered through fritted glass to remove sodium oxide. The concentration of the stock amalgam, solution No. 1, Table I, was determined gravimetrically and checked by the gasometric method based on the

amount of hydrogen evolved from the reaction of the sodium amalgam with hydrochloric acid. Concentrations of the remaining solutions were determined gravimetrically by successive dilution of the stock amalgam.

The sample and amalgams were placed in a cell which permitted exclusion of the atmosphere, Fig. 30. A pressed pellet of the PEO·NaSCN complex,4.5:1, was fitted into an o-ring which was then clamped between the side arms. All loading of the polymer complex was carried out in a nitrogen filled dry box. One side arm was filled with the stock amalgam solution while the other was successively filled with the dilutions of the stock. Introduction of amalgam solutions was done with a gas-tight syringe under a flush of dry nitrogen.

The potentials of the cell were measured using a Keithley multimeter together with an electrometer containing an RCA CA3140 E MOS/FET operational amplifier designed to increase the input impedance of the measuring device to 10^{12} ohms. All measurements were made at room temperature, $23.5 \pm 0.2\ ^{o}C$, which was monitored using an iron-constantan thermocouple and millivolt meter. The cell and connecting leads were placed in an aluminum box designed to shield the system from extraneous radiation. Reversing the cell polarity produced insignificant changes in the magnitude of the observed potentials. The emf was read after the potential had maintained a stable (± 0.3 mV) value over a period of one hour. Typical stabilization times were of the order of one to two hours. The measured results are given in Table I. As a check on these measurements, emf values were determined on a different batch of the polymer electrolyte using different amalgam preparations. Agreement between the data sets was good.

A value of the cell impedance was obtained by loading standard resistors in parallel with the cell and observing the change in emf. The observed room temperature cell impedance of $3.0 \times 10^{6}\ \Omega$ was well within the capability of the measuring device and yielded a D.C. conductivity of $6.3 \times 10^{-8} (\Omega\ cm)^{-1}$, which is in general agreement with the A.C. value shown by armand.[29]

The emf of the concentration cell Hg-Na(x_1)| PEO·NaSCN | Hg-Na(x_2) is expressed by[33]

$$E_{obs} = (1 - t_e)E_{id} = (1 - t_e)\frac{RT}{nF} \ln \frac{a_1}{a_2} = (1 - t_e)\frac{RT}{nF} \ln \frac{\gamma_1 x_1}{\gamma_2 x_2}$$

The activity coefficients for dilute amalgams (present case) may be calculated from the relationship[35]

$$\text{Log } \gamma = Qx$$

where

$$Q = 18.720 - 8.00 \times 10^{-3} T$$

From this, E_{id} may be calculated:

$$E_{id} = \frac{RT}{F} 2.303 \log \frac{x_1}{x_2} + \frac{RT}{F} 2.303 Q(x_1 - x_2)$$

A plot of E_{obs} vs. E_{id} for each x_2 (x_1 being fixed as the stock amalgam, solution No. 1) yields a straight line (Fig. 31) of slope $(1-t_e)$.

For a purely ionic conductor the value of $(1 - t_e)$ should be unity. Least-squares treatment of E_{obs} vs. E_{id} produced a line of slope 1.005 ± 0.005, Fig. 31. This result establishes that the electronic contribution to the total electrical conductivity of PEO·NaSCN is negligible and that the ionic component is responsible for the conduction. Since sodium-reversible electrodes were employed and since the conductivity is close to the published ac data, the sodium ion is implicated as the major charge in the PEO·NaSCN complex.

Definition of variables:

E_{obs} = measured emf

t_e = electronic transference number

E_{id} = ideal emf, value of E_{obs} when $t_e = 0$

R = universal gas constant

T = absolute temperature

n = number of electrons transferred

F = Faraday constant

a_1, a_2 = activities of sodium in the amalgams

γ_1, γ_2 = activity coefficients of sodium in the amalgams

x_1, x_2 = mole fractions of sodium in the amalgams

Table I. Ideal and observed emf's of concentration cell at room temperature.

Solution No.	x_{Na}	E_{id}(mV)	E_{obs}(mV)
1	0.04103	-	-
2	0.03426	11.13	10.98
3	0.02944	19.64	19.47
4	0.02406	29.99	29.11
5	0.01928	40.25	40.89
6	0.01440	52.36	52.10
7	0.009477	67.84	68.34
8	0.004753	90.00	89.83

We have also used infrared and Raman spectroscopy to study well-characterized samples of the following polymer/salt complexes: PEO·NaBr, PEO·NaI, PEO·NaSCN, PEO·$NaBF_4$, PEO·$NaCF_3SO_3$, PEO·KSCN, PEO·RbSCN, and PEO·CsSCN. Cation-dependent vibrational bands observed in the far infrared and M-O_n symmetric stretching bands observed in the Raman support a cation-oxygen atom interaction, and indicate the polyether chain may wrap around the cations. The NaX and KX complexes in particular are believed to be in a new helical conformation similar to pure PEO.

6. Effects of Impurities on Ionic Conductivity in Sodium β″-Alumina

Personnel: Y.-T. Tsai, Ph.D. Candidate

Calcium is a common impurity present in the starting materials such as $LiNO_3$, Na_2CO_3, etc. which are commonly employed in the fabrication of sodium β″-alumina. Accordingly, a study of the effect of Ca impurities on the ionic conductivity of sodium β″-alumina is important technologically as well as representing a very interesting and challenging scientific problem

because there are several possible locations for the Ca^{2+} ions in the β″-alumina lattice and each should have its own effect on the resulting ionic conductivity. For instance, it is possible that:

(1) Ca^{2+} may occupy the vacant Na^{+} ion sites on the conduction planes and, if the vacancy possesses a virtual charge (relative to the lattice), it may also form a dipolar complex with a near-neighbor sodium vacancy, both possibilities leading to a decrease in the bulk Na^{+} ion conductivity;

(2) Ca^{2+} may also be segregated, or even precipitated as a Ca-rich second phase, at/or near the grain boundary and form a nonconductive layer in such locations, thereby decreasing the grain boundary conductivity.

Last year, we reported on the results of some experiments which dealt with the effects of CaO additions on the conduction behavior of polycrystalline sodium β″-alumina samples prepared in our laboratories. While there were adverse effects of Ca on both the Na^{+} ion conduction within the bulk and at the grain boundaries, the grain boundary conductivity showed a much more pronounced dependence on the CaO concentration than does the bulk conductivity. As a follow-up, we initiated some experiments on the effects of ion-exchanging Ca^{2+} ions for some (or all) of the Na^{+} ions in single crystal β″-alumina. The results (reported below) of these experiments are very interesting, but are not yet fully understood by us.

Single crystals of pure calcium and mixed calcium-sodium β″-alumina were prepared by ion-exchange techniques. A small single crystal of sodium β″-alumina (MgO-stabilized sample measuring 2.635 x 1.480 x 0.695 mm^3) was immersed in the molten eutectic mixture of $Ca(NO_3)_2$ and $CaCl_2$ [$Ca(NO_3)_2$: $CaCl_2$ = 58.33 m/o : 41.67 m/o; eutectic temperature - 409°C] at 512.5 ± 2.5°C for 3 days. The sodium content in the bath was determined to be 1.16 w/o by flame-emission spectroscopy. The crystal delaminated along the conduction plane into two small crystals. Both crystals were transparent after ion-exchange. One of the crystals (crystal A) was selected for conductivity measurements, while the other (crystal B) was immersed in a new ion-exchange bath at 510 ± 5°C for 3 days. The sodium content of the bath after this exchange was measured to be 5.84 w/o of the original sodium β″-alumina. The total sodium content exchanged after the second experiment was calculated to

be 7.00 w/o, indicating that the exchange was complete. The compositions of these ion-exchanged samples are summarized in Table II.

The ionic conductivities of partially- and completely-exchanged samples were measured as functions of temperature using sputtered gold electrodes and a dry nitrogrn atmosphere. The conductivity data were collected with our automated analyzer system and were corrected for the inductance of the measuring lead wires. These data were analyzed by means of complex admittance plots which displayed a single semicircular arc over the frequency range of 100 Hz to 500 kHz. The bulk conductivity was calculated from the high-frequency intercept of the real axis of the complex admittance plot. Both partially- and completely-exchanged samples followed an Arrhenius behavior between 250° and 470°C (see Figs. 32 and 33). The activation energies were calculated to be 0.609 eV for the partially-exchanged sample and 0.574 eV for the completely-exchanged one. The conductivity results are summarized in Table III.

Table II. Compositions of Calcium Ion-Exchanged β″-aluminas.*

Sample	Composition
Na β″-alumina	$0.927\ Na_2O \cdot 0.854\ MgO \cdot 5.073\ Al_2O_3$
A	$0.774\ Na_2O \cdot 0.153\ CaO \cdot 0.854\ MgO \cdot 5.073\ Al_2O_3$
B	$0.927\ CaO \cdot 0.854\ MgO \cdot 5.073\ Al_2O_3$

*This calculation is based on the assumption that each Ca^{2+} ion substitutes for two Na^{+} ions in the conduction plane to satisfy the electroneutrality condition.

Table III. Ionic Conductivities of Calcium-Exchanged β″-aluminas.

Sample	$\sigma(300^{o}C)$	ΔE_a (eV)	$\sigma_o(^{o}K\ \Omega^{-1}cm^{-1})$
A	2.47×10^{-3}	0.609	3.20×10^{5}
B	3.92×10^{-3}	0.574	2.50×10^{5}

Figure Captions

Fig. 1 - Comparison of ionic conductivities for the same LiI-fused silica composite after being heat-treated in three different manners. The term "annealed" refers to conductivity data recorded as the composite was cooled from the melt to 20°C. The three curves are normalized by taking the ratio of the composite conductivity to the conductivity of a sample receiving the same treatment but containing no particles.

Fig. 2 - Apparatus used to generate cooling curves and record the complex impedance of hydrated lithium iodide.

Fig. 3 - Lithium iodide-water phase diagram. Dotted lines are drawn by extrapolation.

Fig. 4 - Complex impedance plot for the equivalent circuit shown.

Fig. 5 - Cooling and resistance curves for the composition $LiI \cdot 1.02\ H_2O$.

Fig. 6 - Conductivity as a function of water content at 28°C.

Fig. 7 - Conductivity as a function of water content at 42°C. Break in slope at $LiI \cdot 1.7\ H_2O$ corresponds to the eutectic composition.

Fig. 8 - Comparison of the ionic conductivity at 42°C for compositions between $LiI \cdot H_2O$ and $LiI \cdot 2H_2O$ with the conductivity predicted by Maxwell's theory and effective-medium theory.

Fig. 9 - Microstructure composed of a random distribution of grains of two materials. Taken from reference 9.

Fig. 10 - Comparison of the ionic conductivity at 42°C for compositions between LiI and $LiI \cdot H_2O$ with the conductivity predicted by Maxwell's theory and effective-medium theory.

Fig. 11 - Comparison of the ionic conductivity at 28°C for compositions between LiI and $LiI \cdot \frac{1}{2}\ H_2O$ with the conductivity predicted by effective-medium theory if $LiI \cdot \frac{1}{2}\ H_2O$ is assumed to exist.

Fig. 12 - Arrhenius plots for dehydrated lithium iodide and $LiI \cdot 0.77\ H_2O$.

Fig. 13 - Arrhenius plots for compositions ranging from dehydrated lithium iodide to the hemi-hydrate.

Fig. 14 - Comparison of the activation energies of ion migration for composition between LiI and $LiI \cdot H_2O$ with the activation energies predicted by Maxwell's theory and effective-medium theory.

Fig. 15 - Comparison of the pre-exponential factor for compositions between LiI and $LiI \cdot H_2O$ with the pre-exponential factors predicted by Maxwell's theory and effective-medium theory.

Fig. 16 - A plot of the natural logarithm of the pre-exponential factor versus the activation energy for compositions between LiI and $LiI \cdot H_2O$ as compared to Maxwell's theory.

Fig. 17 - A plot of the natural logarithm of the pre-exponential factor versus the activation energy for compositions between LiI and $LiI \cdot H_2O$ as compared to effective-medium theory.

Fig. 18 - Cell configuration for conductivity measurements with reversible liquid electrodes.

Fig. 19 - Equivalent circuit for the measurement of the conductivity of reversible liquid electrodes.

Fig. 20 - Schematic complex admittance plot for reversible liquid electrodes.

Fig. 21 - Equivalent circuit and schematic complex admittance diagram for the cell: reversible liquid electrode|NASICON|reversible liquid electrode.

Fig. 22 - Admittance plot for a solution of sodium iodide in propylene carbonate.

Fig. 23 - Admittance plot for NASICON with sodium reversible electrodes.

Fig. 24 - (A) Equivalent circuit for the cell: ion-blocking electrode|NASICON|ion-blocking electrode.

(B) Schematic complex admittance plot for the circuit shown in (A).

Fig. 25 - Complex admittance plot at 240°C for the cell: Au|NASICON|Au.

Fig. 26 - Plot of $\ell n\ (G_b T)$ versus $1/T^{\circ}K$ for the cell: graphite|NASICON|graphite.

Fig. 27 - Comparison of the present conductivity results on NASICON with those of other investigators.

Fig. 28 - Plot of $\ell n\ G_b T$ versus $1/T^{\circ}K$ for the fast protonic conductor NH_4^+ - β''-gallate.

Fig. 29 - Raman spectrum at 25°C for the fast protonic conductor NH_4^+ - β-gallate.

Fig. 30 - Schematic drawing of the cell utilized in the Na^+ ion transference number measurements in the polymer complex PEO·NaSCN.

Fig. 31 - Plot of the observed cell voltage for the complex PEO·NaSCN versus the "ideal" voltage at 25°C obtained in the transference number measurements.

Fig. 32 - Plot of $\ell n\, \sigma T$ versus $1/T^{\circ}K$ for the partially-exchanged single-crystal sample with the nominal composition 0.774 NaO·0.153 CaO·0.854 MgO·5.073 Al_2O_3.

Fig. 33 - Plot of $\ell n\, \sigma T$ versus $1/T^{\circ}K$ for the completely-exchanged single-crystal sample with the nominal composition 0.927 CaO·0.854 MgO·5.073 Al_2O_3.

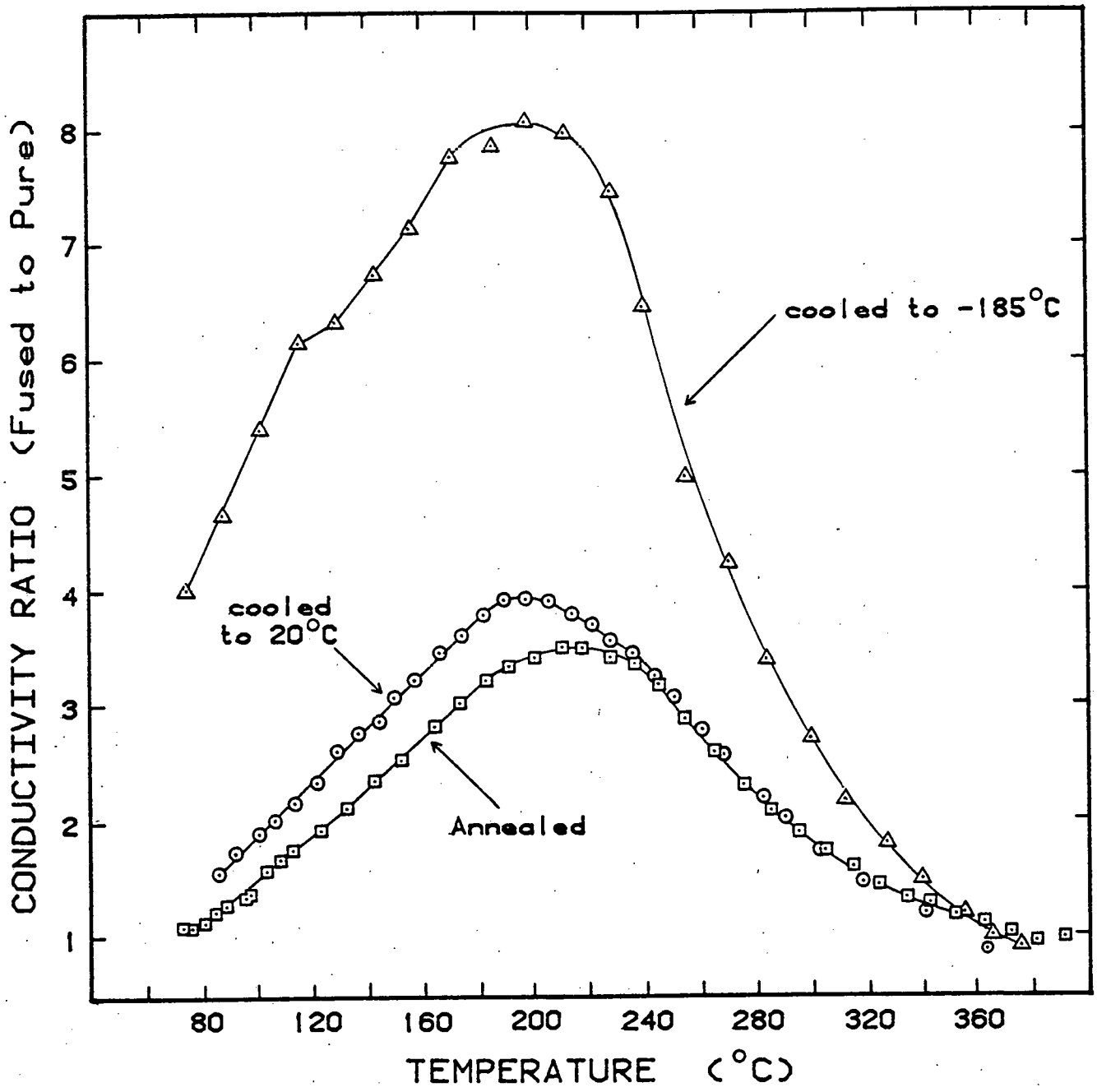
CONDUCTIVITY RATIO (Fused to Pure)
8
7
6
5
4
3
2
1
cooled to -185°C
cooled to 20°C
Annealed
80
120
160
200
240
280
320
360
TEMPERATURE (°C)

Figure 1

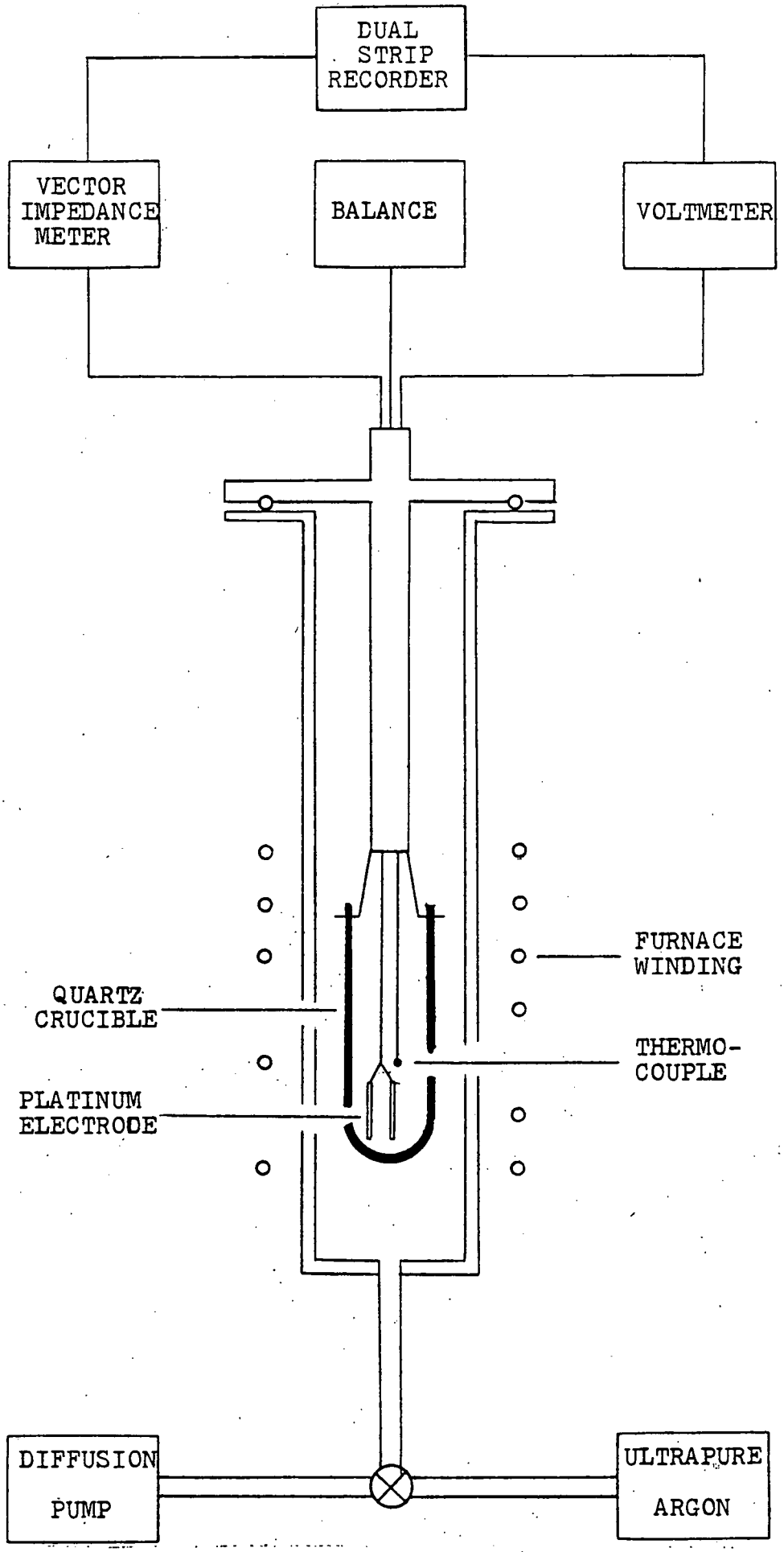
DUAL
STRIP
RECORDER
VECTOR
IMPEDANCE
METER
BALANCE
VOLTMETER
FURNACE
WINDING
QUARTZ
CRUCIBLE
THERMO-
COUPLE
PLATINUM
ELECTRODE
DIFFUSION
PUMP
ULTRAPURE
ARGON

Figure 2

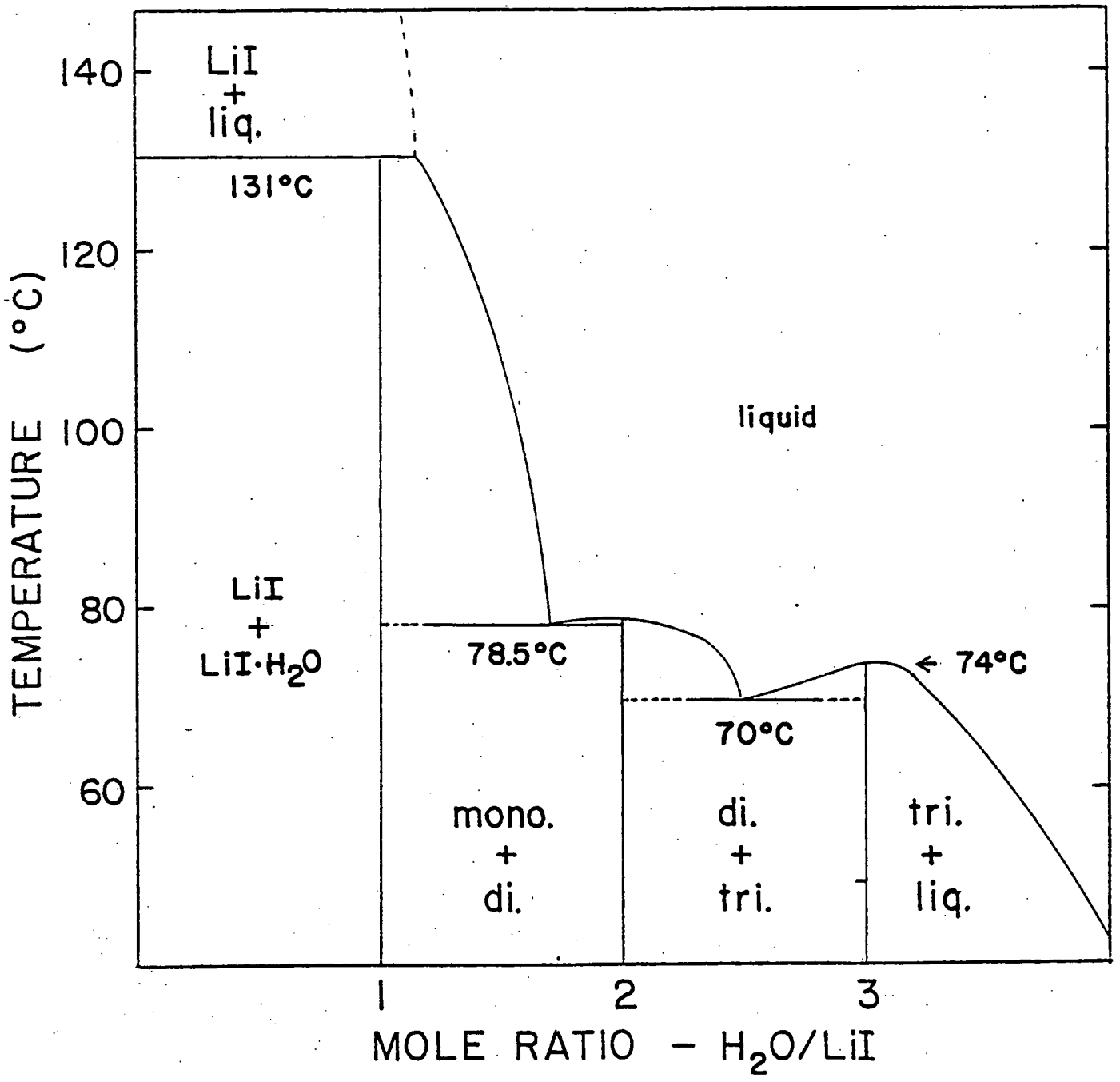
140
120
100
80
60
TEMPERATURE (°C)
LiI
+
liq.
131°C
liquid
LiI
+
LiI·H2O
78.5°C
← 74°C
70°C
mono.
+
di.
di.
+
tri.
tri.
+
liq.
1
2
3
MOLE RATIO – H2O/LiI

Figure 3

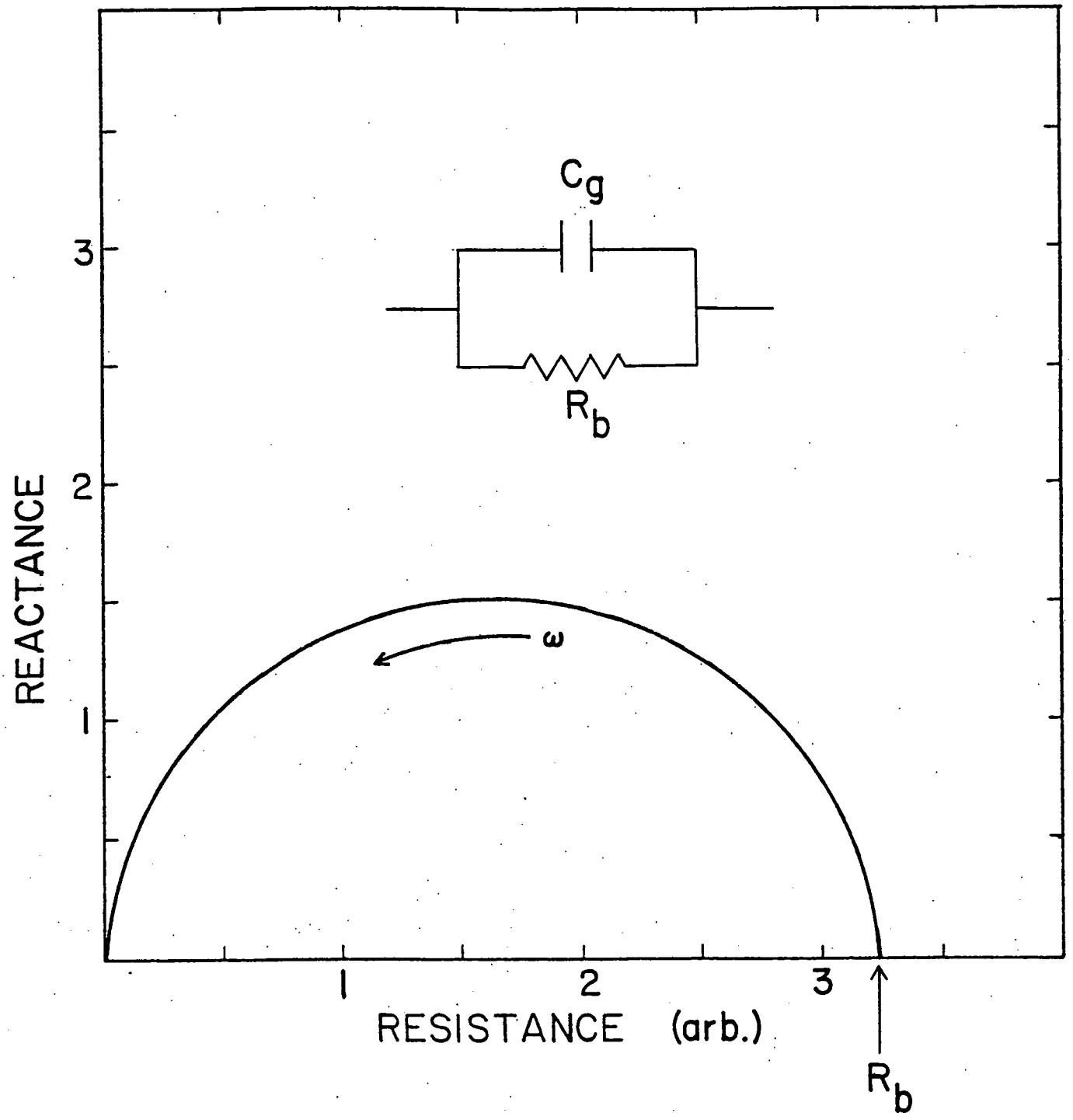

Figure 4

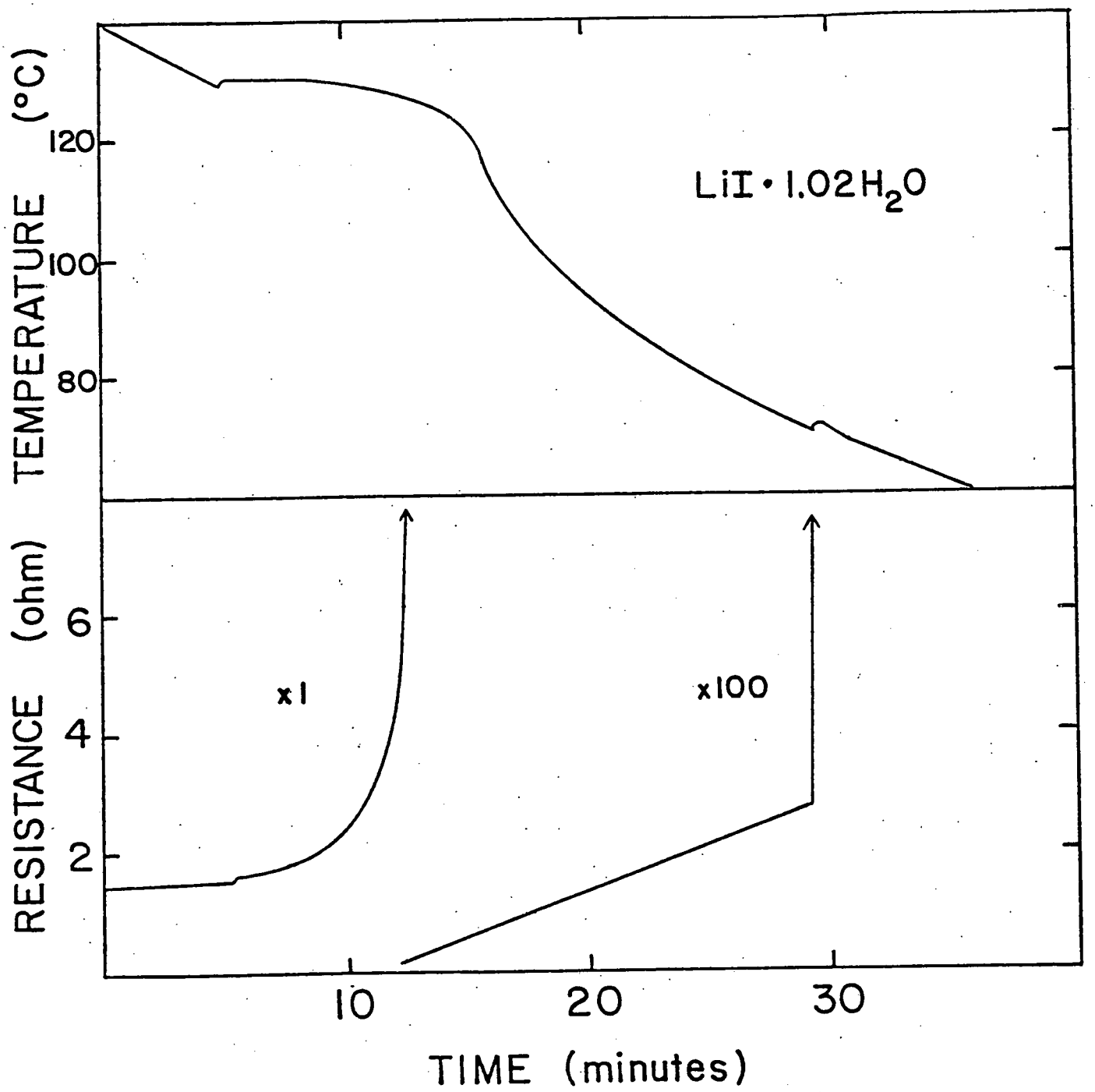
TEMPERATURE (°C)
120
100
80
LiI • 1.02H2O
RESISTANCE (ohm)
6
4
2
x1
x100
10
20
30
TIME (minutes)

Figure 5

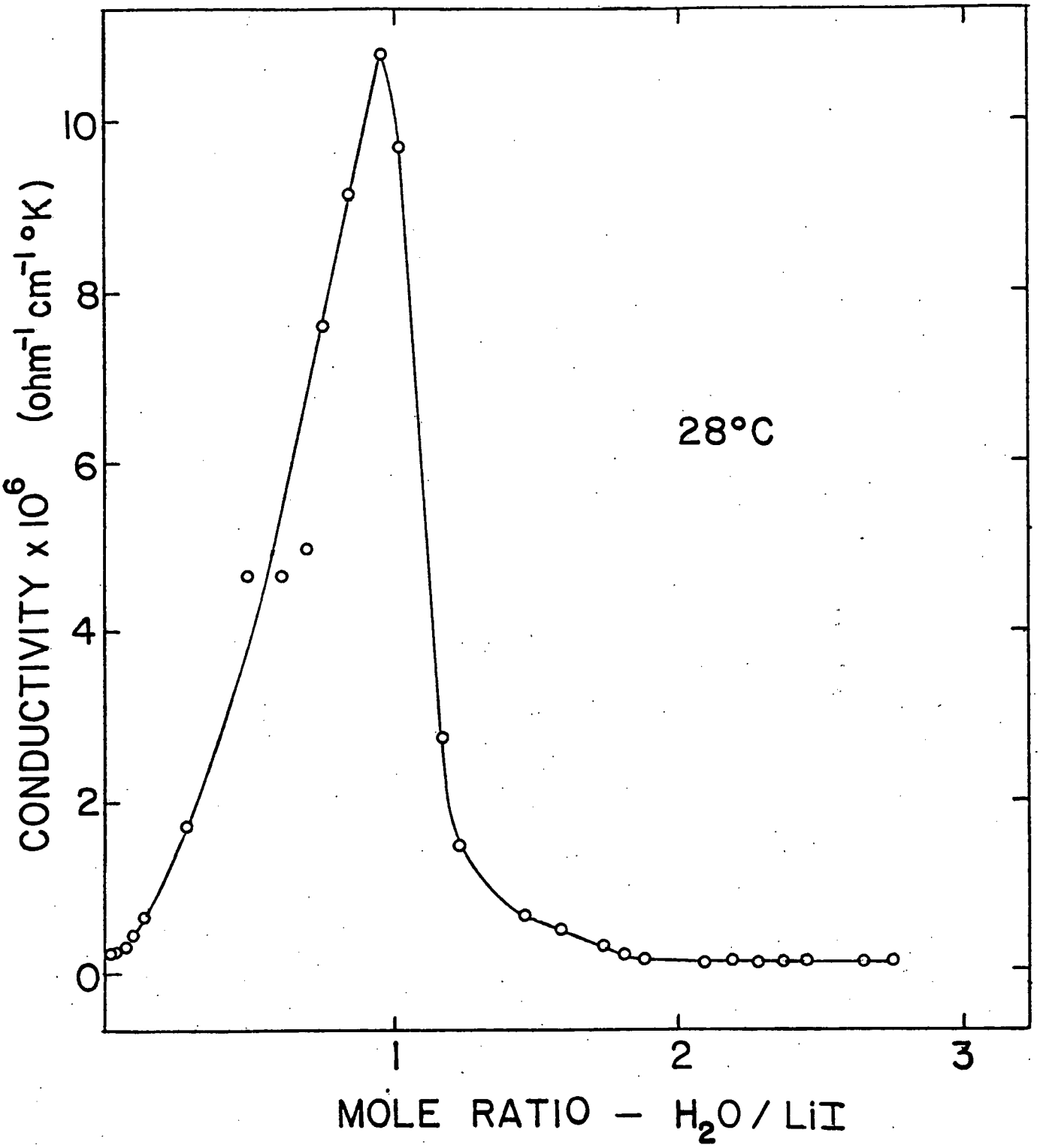
CONDUCTIVITY x 10^6 (ohm^-1 cm^-1 °K)
10
8
6
4
2
0
28°C
1
2
3
MOLE RATIO – H2O / LiI

Figure 6

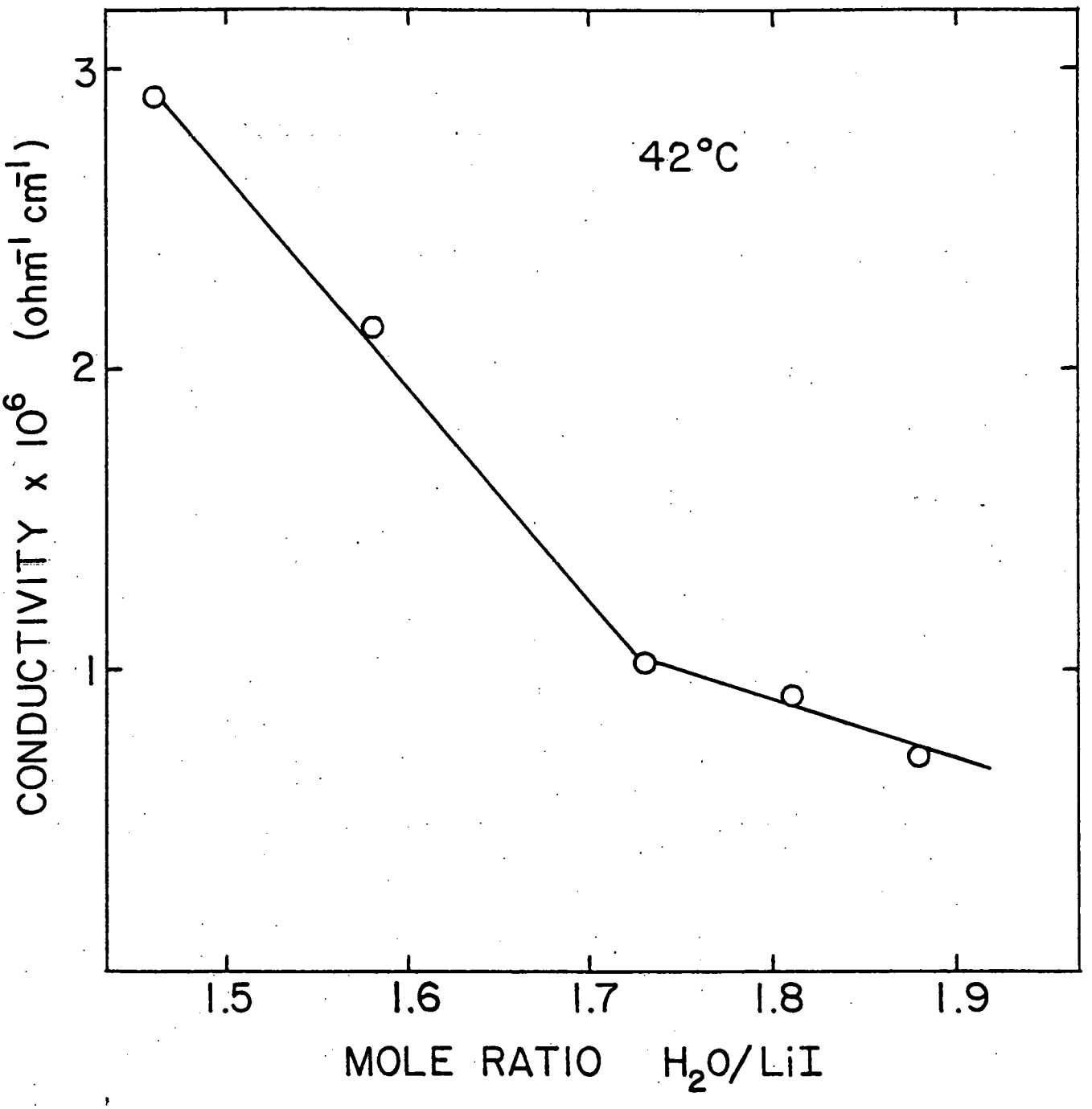
42°C
CONDUCTIVITY x 10^6 (ohm^{-1} cm^{-1})
3
2
1
1.5
1.6
1.7
1.8
1.9
MOLE RATIO H_2O/LiI

Figure 7

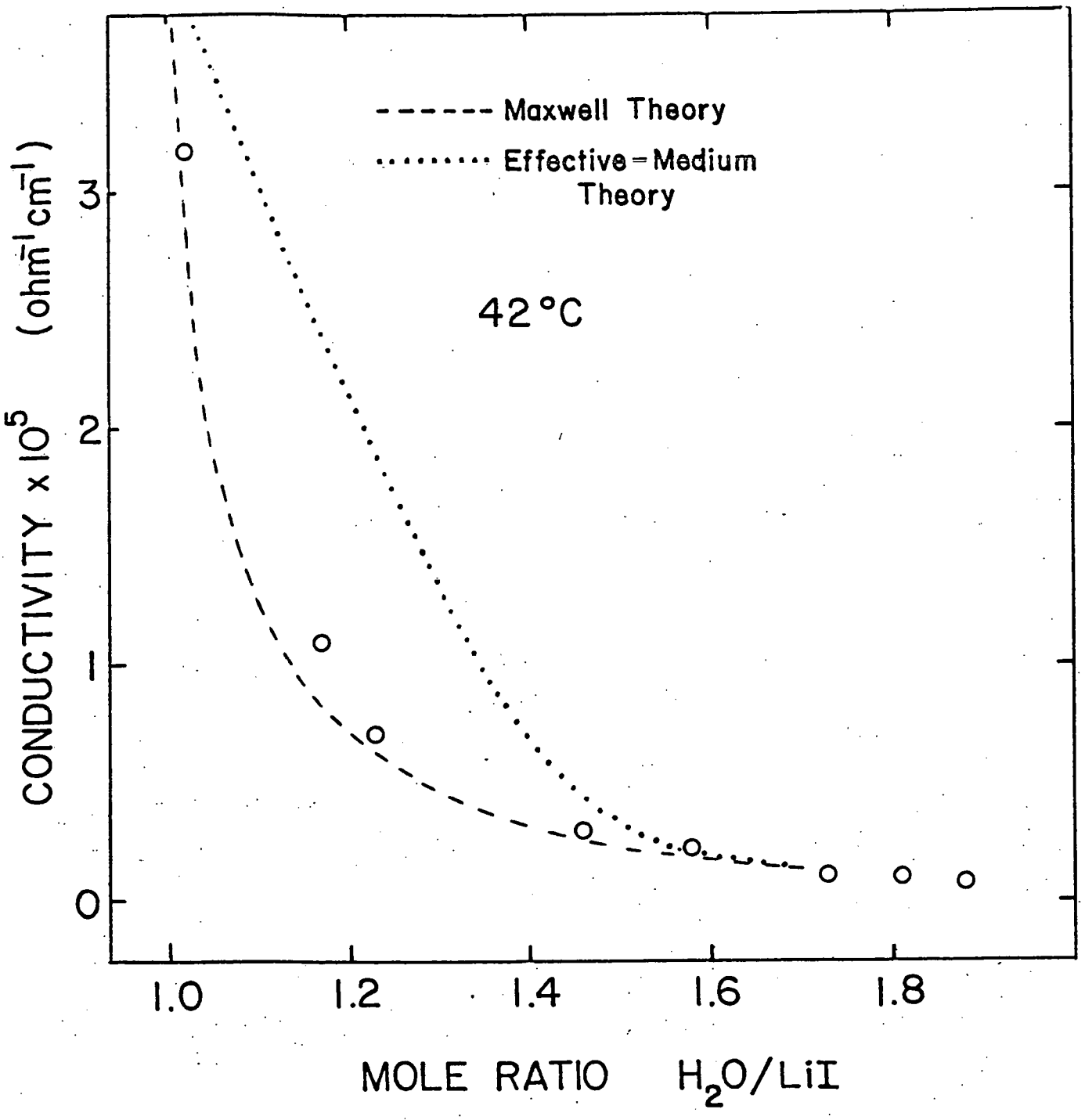
Maxwell Theory
Effective = Medium Theory
42 °C
CONDUCTIVITY x 10^5 (ohm^-1 cm^-1)
0
1
2
3
1.0
1.2
1.4
1.6
1.8
MOLE RATIO H2O/LiI

Figure 8

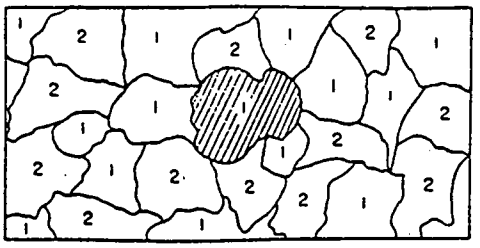

FIG. 1. The shaded crystal of type 1 is surrounded by crystals of both types which are imagnined to be replaced by a single medium of uniform conductivity.

Figure 9

(from ref. 9)

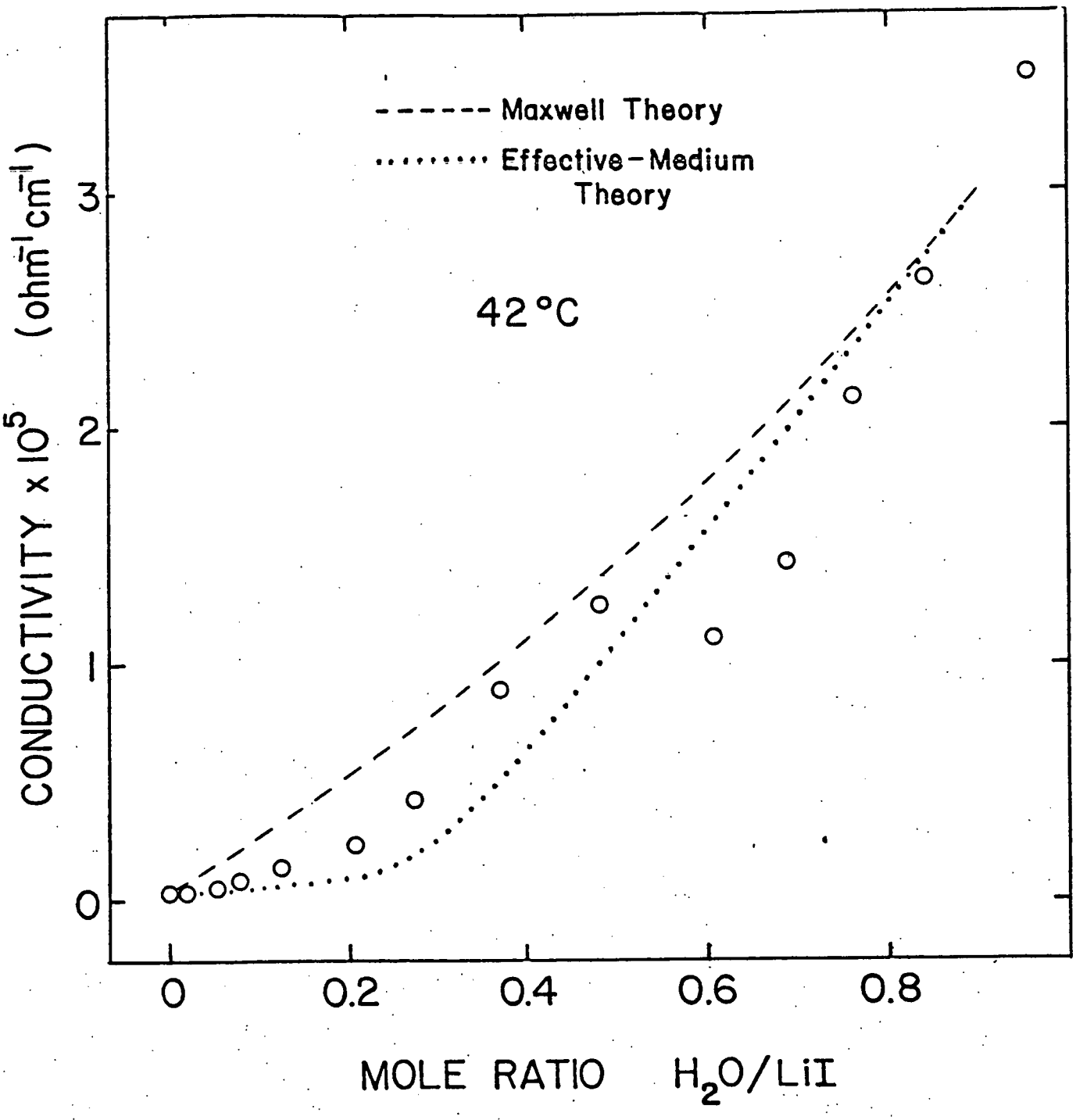
Maxwell Theory
Effective-Medium Theory
42 °C
CONDUCTIVITY x 10^5 (ohm^-1 cm^-1)
0
1
2
3
0
0.2
0.4
0.6
0.8
MOLE RATIO H2O/LiI

Figure 10

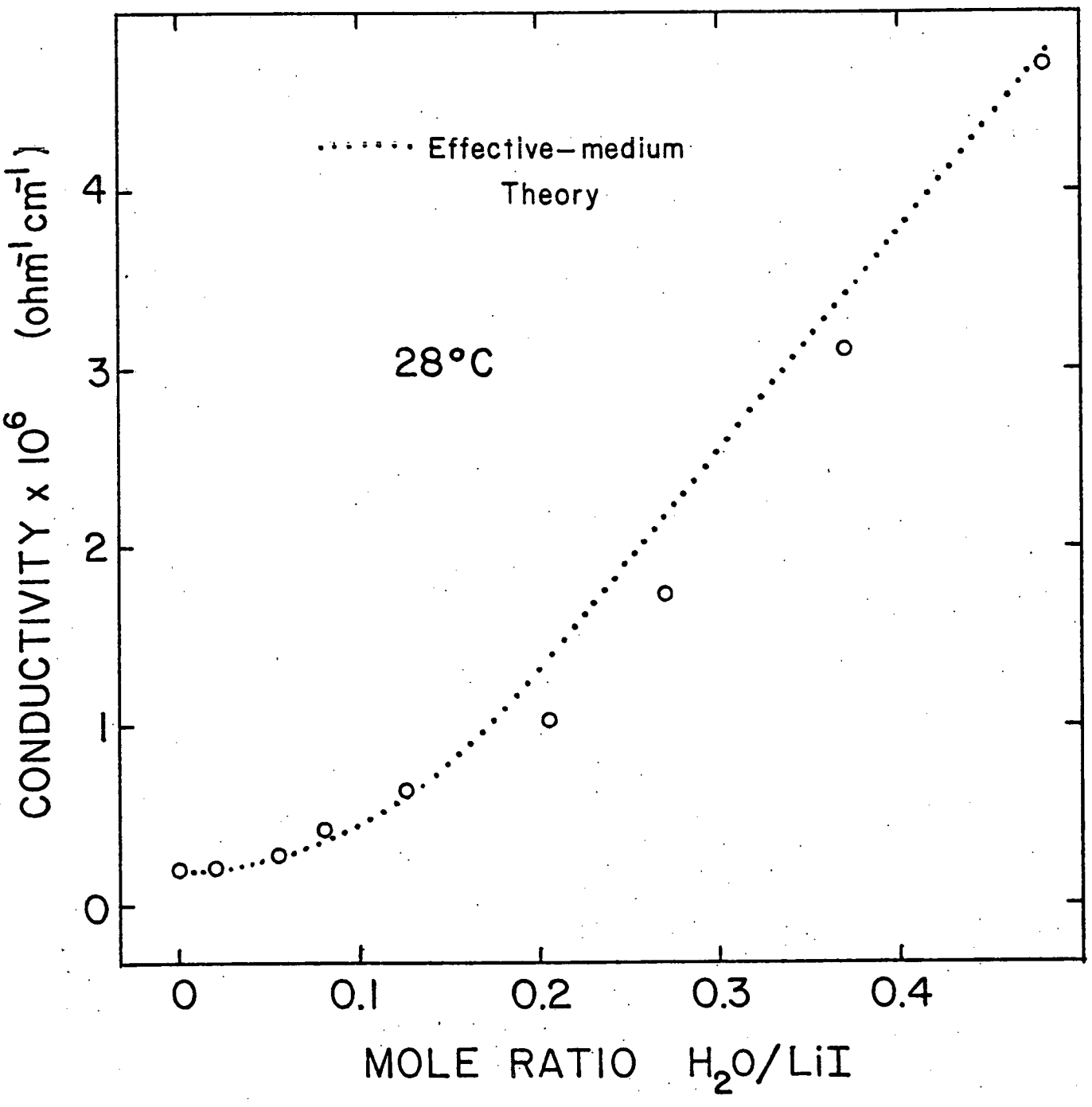
Effective–medium
Theory
28°C
CONDUCTIVITY x 10^6 ($ohm^{-1}cm^{-1}$)
0
1
2
3
4
0
0.1
0.2
0.3
0.4
MOLE RATIO H_2O/LiI

Figure 11

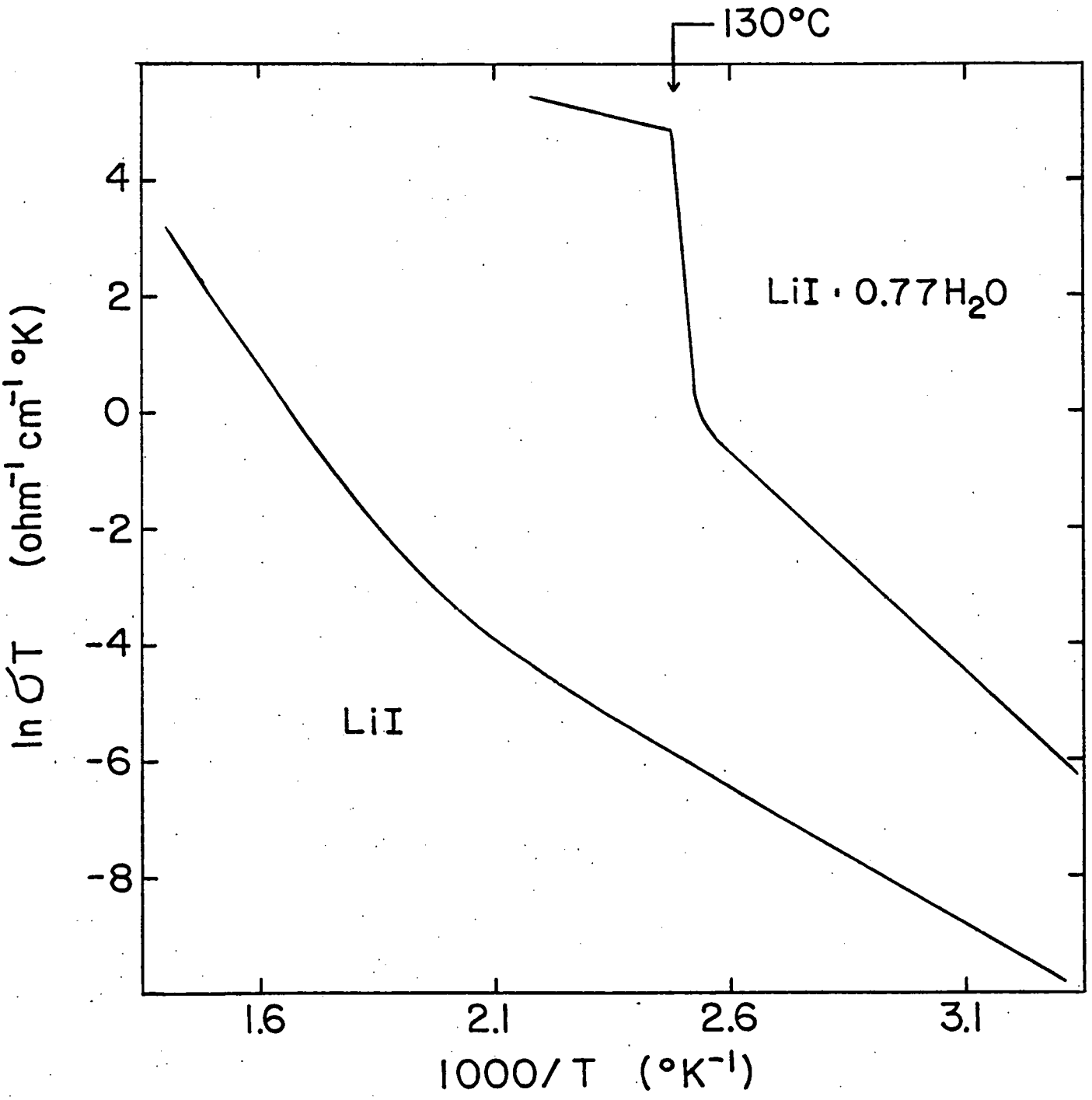
130°C
4
2
0
-2
-4
-6
-8
ln σT (ohm⁻¹ cm⁻¹ °K)
LiI · 0.77H₂O
LiI
1.6
2.1
2.6
3.1
1000/T (°K⁻¹)

Figure 12

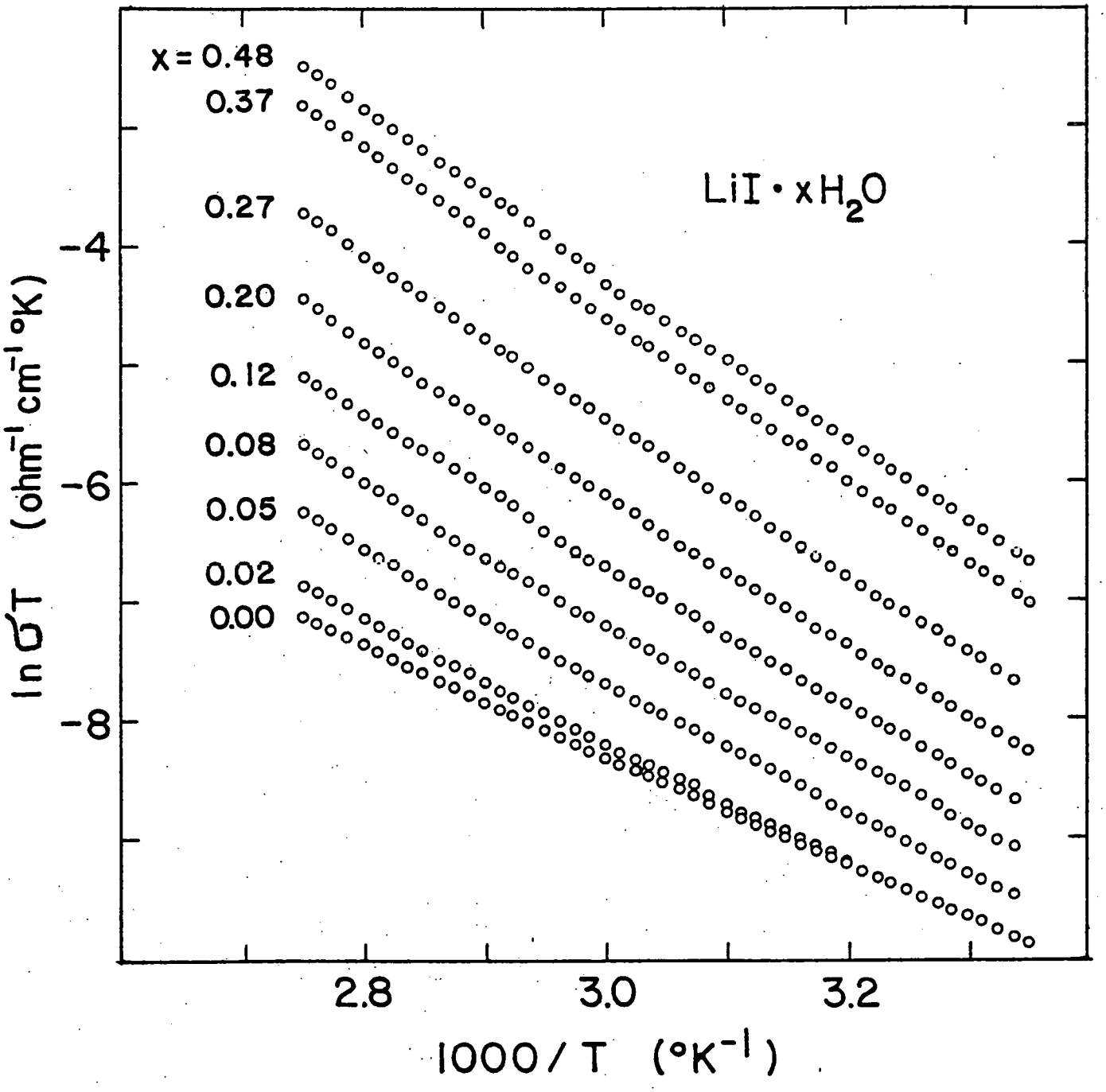
x = 0.48
0.37
0.27
0.20
0.12
0.08
0.05
0.02
0.00
LiI • xH2O
-4
-6
-8
ln σT (ohm-1 cm-1 °K)
2.8
3.0
3.2
1000 / T (°K-1)

Figure 13

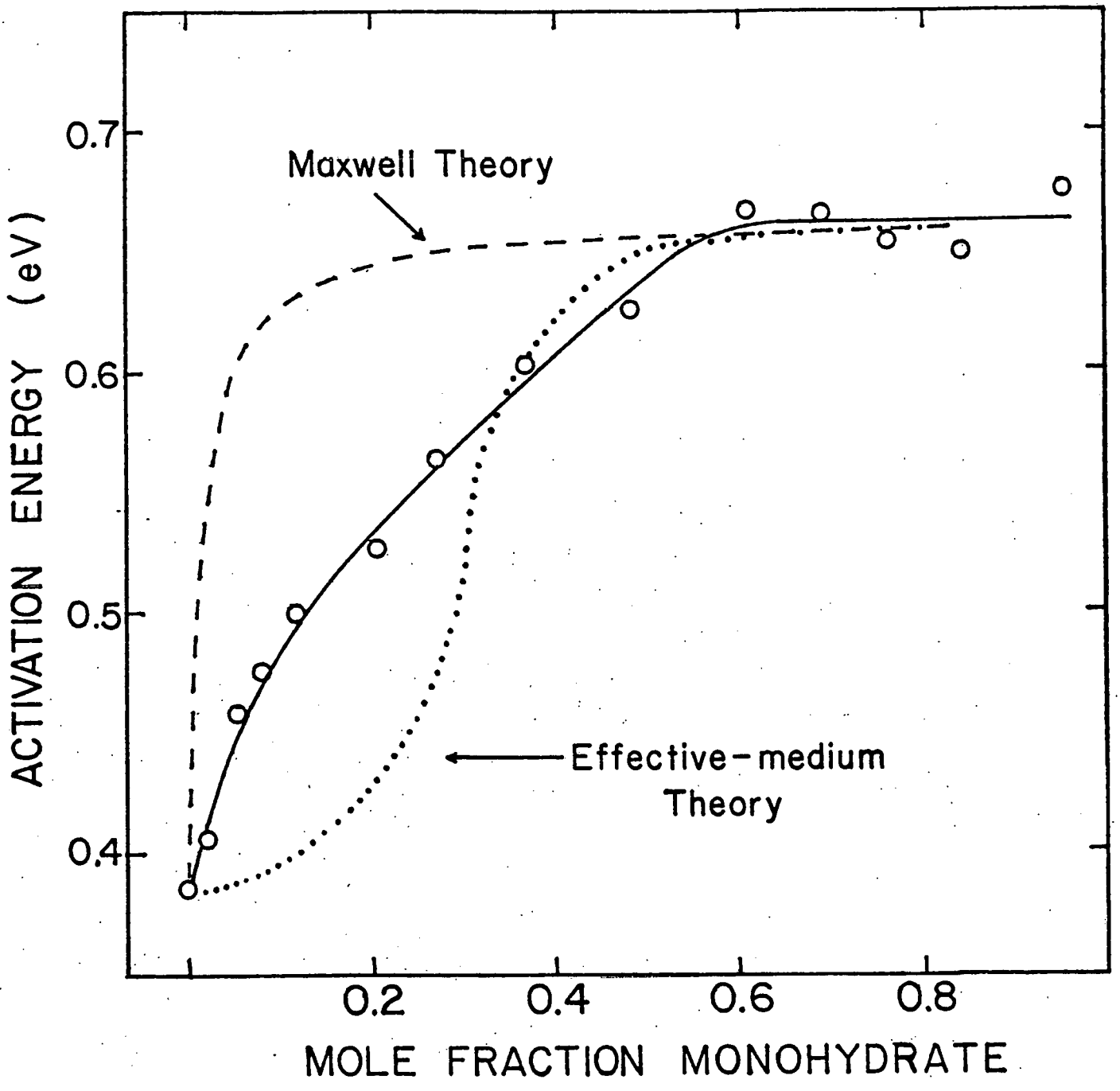
Maxwell Theory
Effective-medium Theory
ACTIVATION ENERGY (eV)
0.7
0.6
0.5
0.4
0.2
0.4
0.6
0.8
MOLE FRACTION MONOHYDRATE

Figure 14

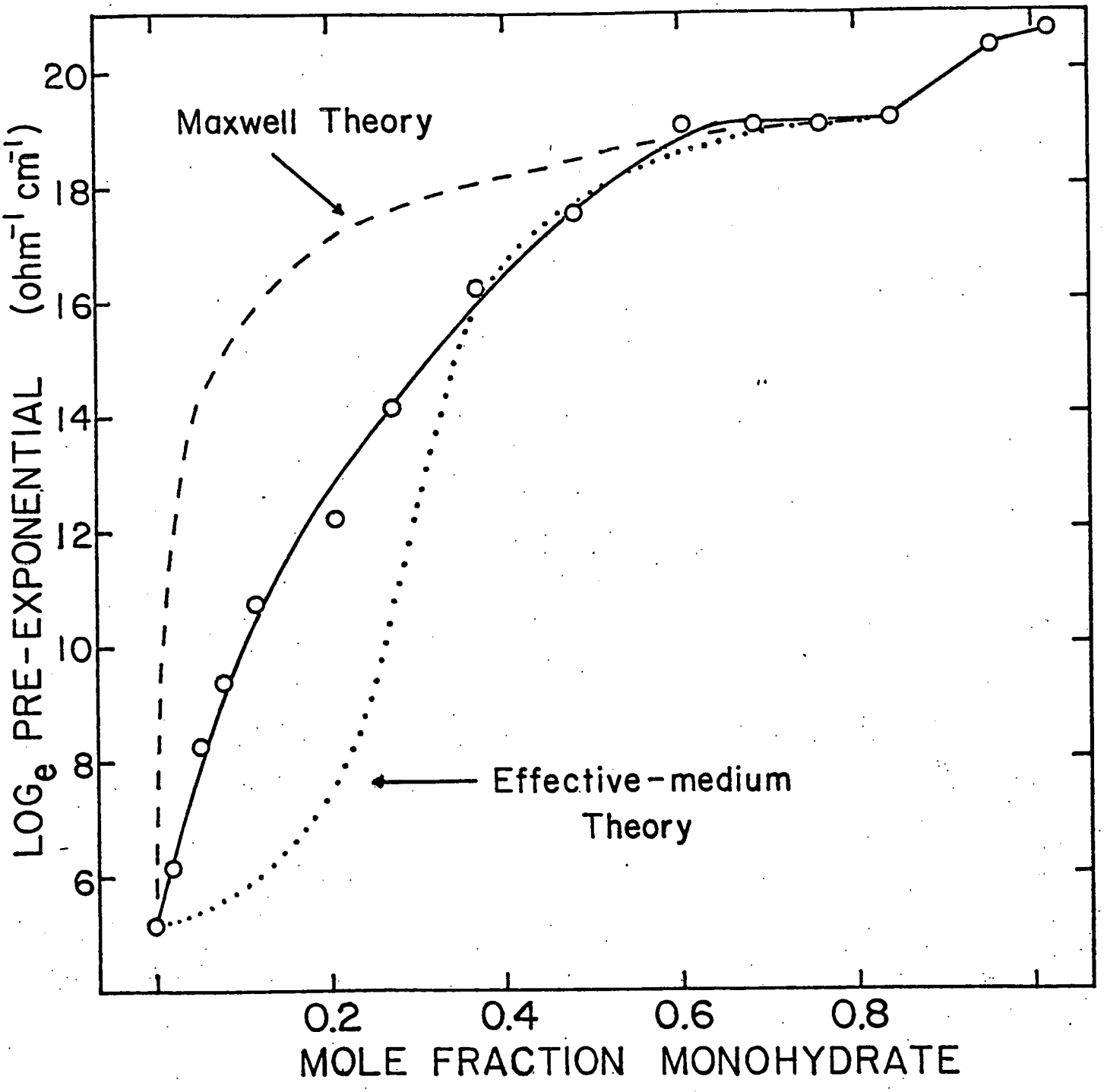
Maxwell Theory
Effective-medium Theory
LOG$_e$ PRE-EXPONENTIAL (ohm^{-1} cm^{-1})
20
18
16
14
12
10
8
6
0.2
0.4
0.6
0.8
MOLE FRACTION MONOHYDRATE

Figure 15

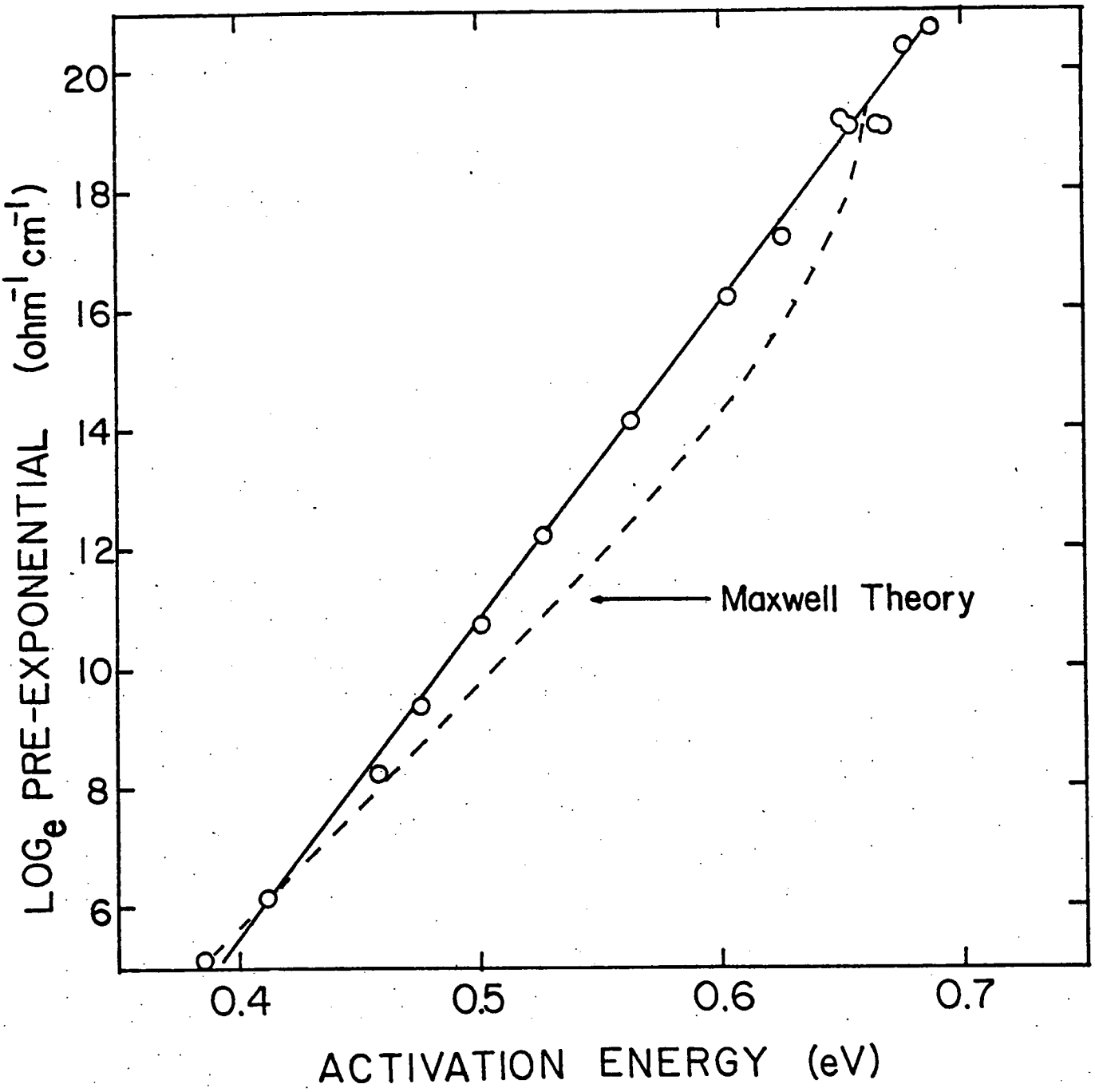
20
18
16
14
12
10
8
6
LOG_e PRE-EXPONENTIAL ($ohm^{-1}cm^{-1}$)
Maxwell Theory
0.4
0.5
0.6
0.7
ACTIVATION ENERGY (eV)

Figure 16

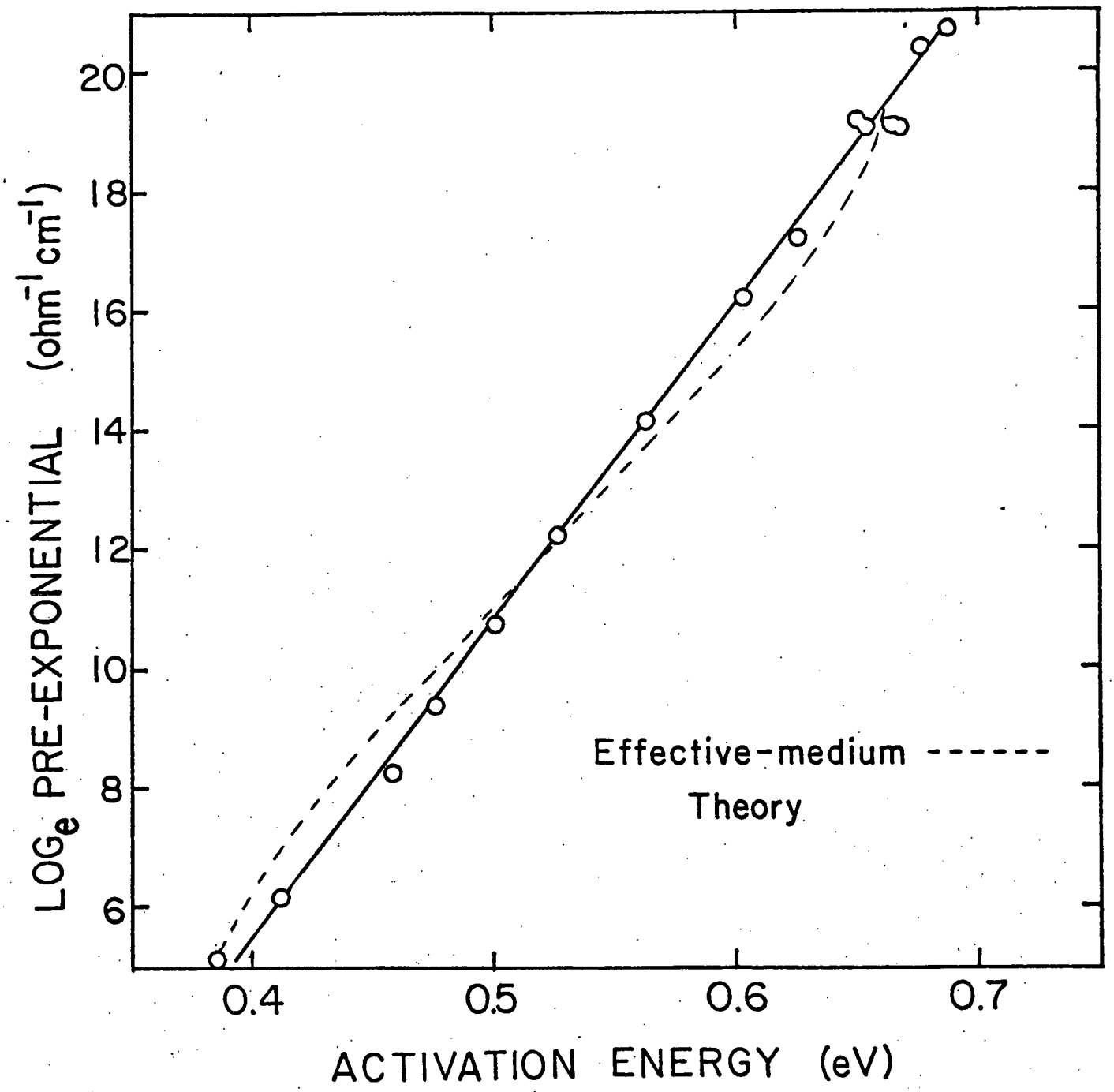
20
18
16
14
12
10
8
6
LOG$_e$ PRE-EXPONENTIAL (ohm^{-1}cm^{-1})
0.4
0.5
0.6
0.7
ACTIVATION ENERGY (eV)
Effective-medium ------
Theory

Figure 17

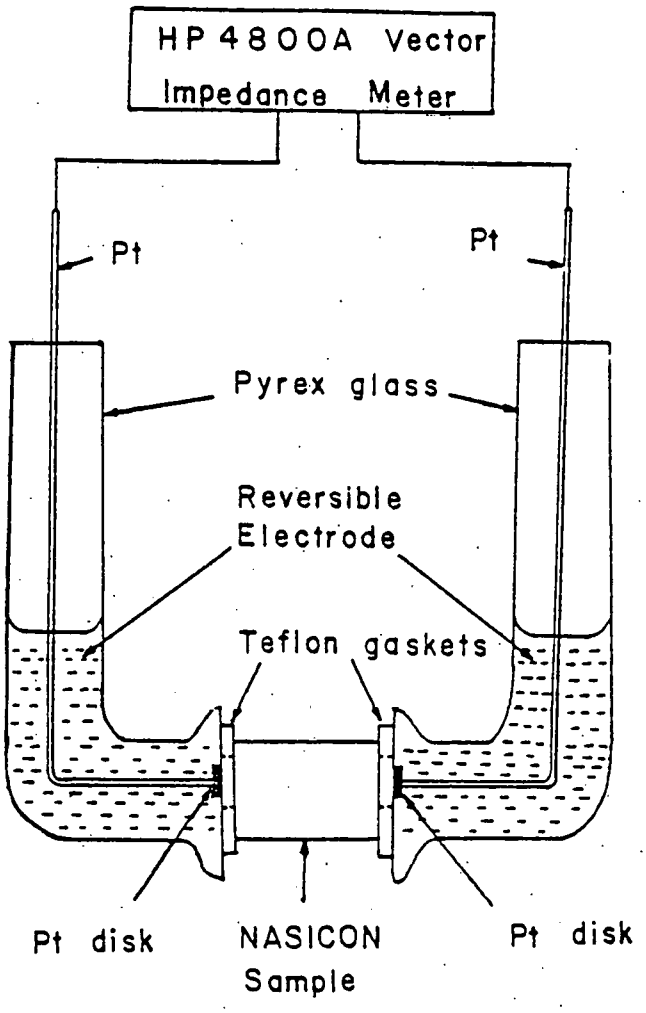
HP 4800A Vector
Impedance Meter
Pt
Pt
Pyrex glass
Reversible
Electrode
Teflon gaskets
Pt disk
NASICON
Sample
Pt disk

Figure 18

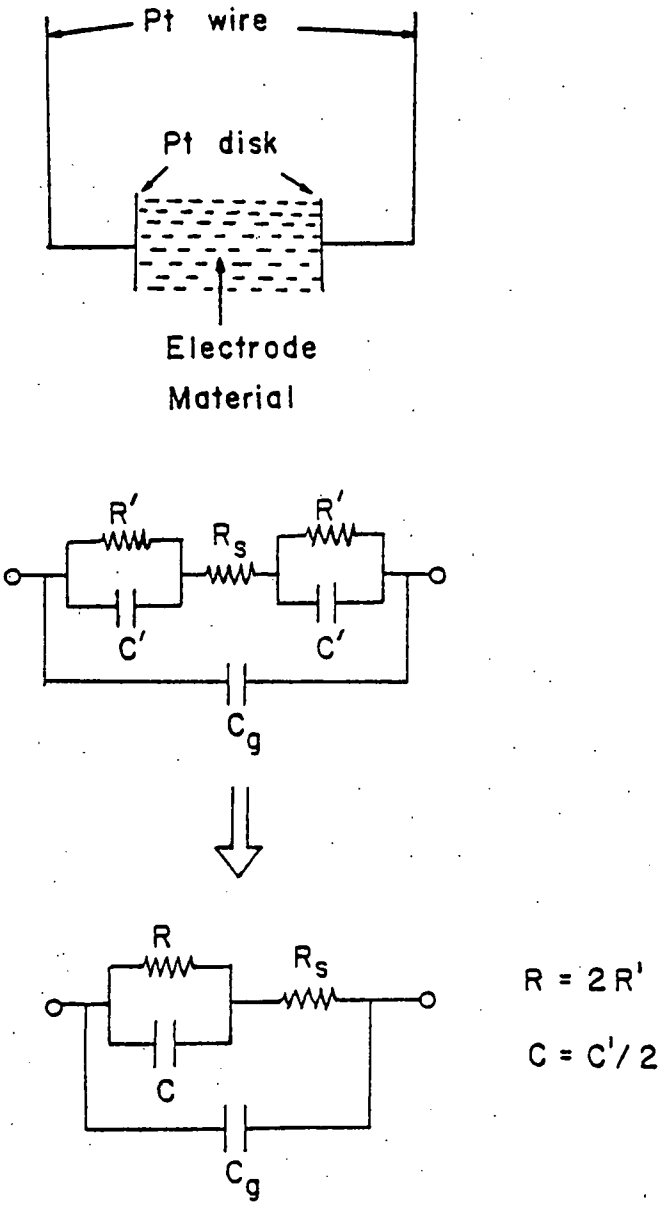

Figure 19

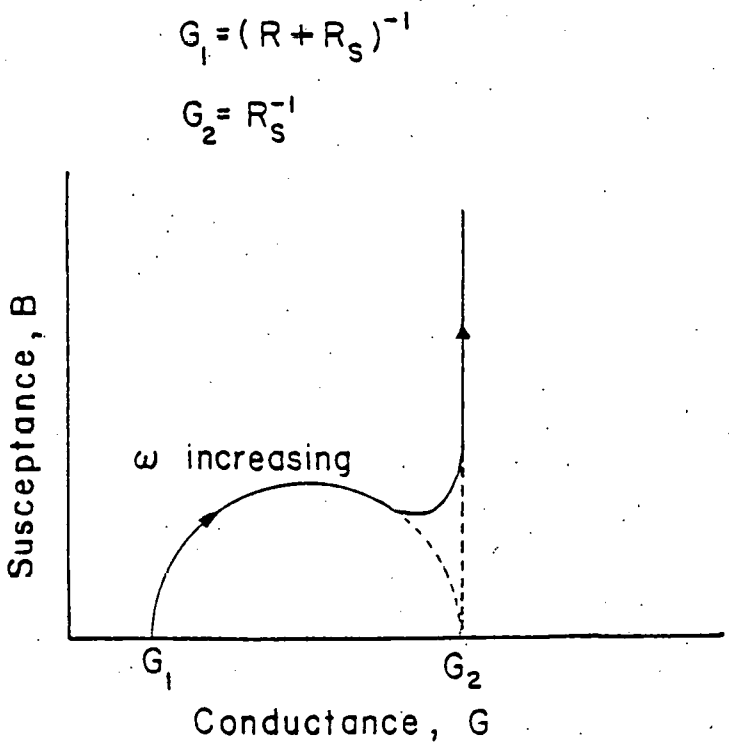
$G_1 = (R + R_s)^{-1}$
$G_2 = R_s^{-1}$
Susceptance, B
ω increasing
G_1
G_2
Conductance, G

Figure 20

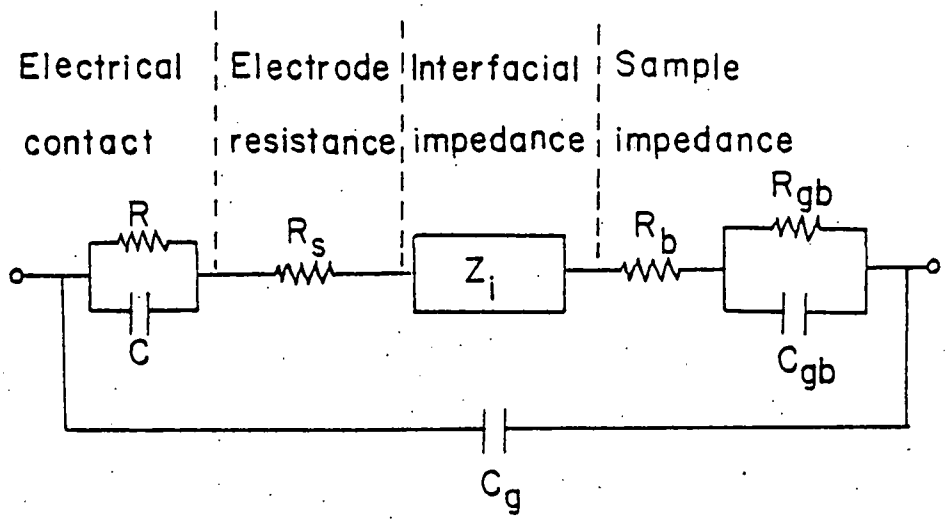

$$G_1 = (R + R_s + R_b + R_{gb})^{-1}$$

$$G_2 = (R_s + R_b + R_{gb})^{-1}$$

$$G_3 = (R_s + R_b)^{-1}$$

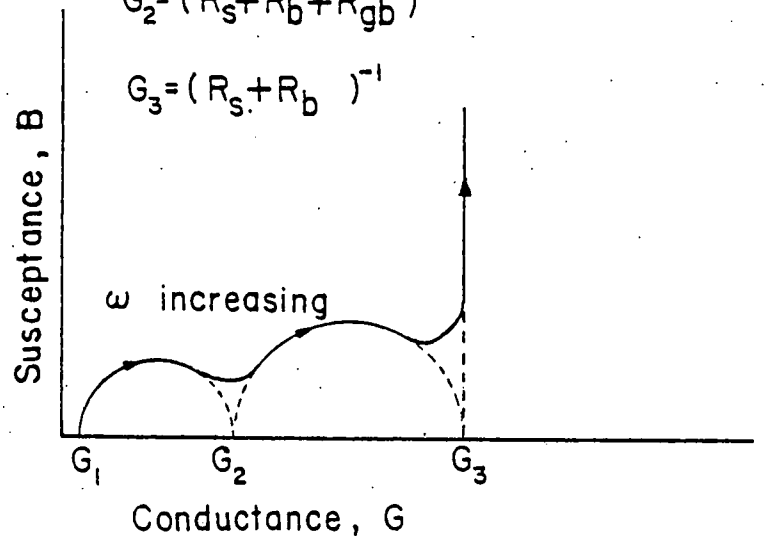

Figure 21

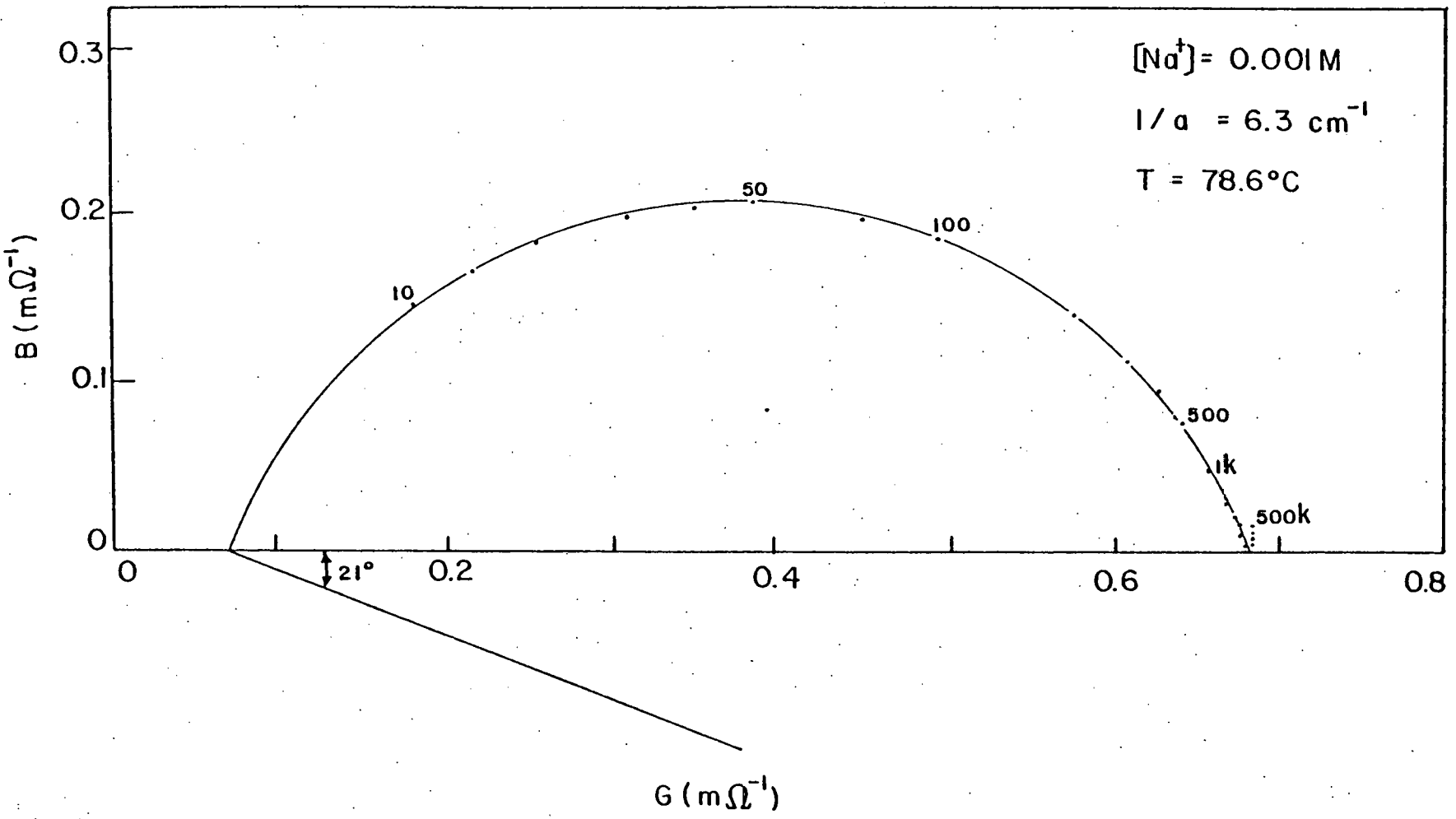
[Na+] = 0.001 M
1/a = 6.3 cm-1
T = 78.6°C
50
100
10
500
1k
500k
21°
0.3
0.2
0.1
0
0
0.2
0.4
0.6
0.8
B (mΩ-1)
G (mΩ-1)

Figure 22

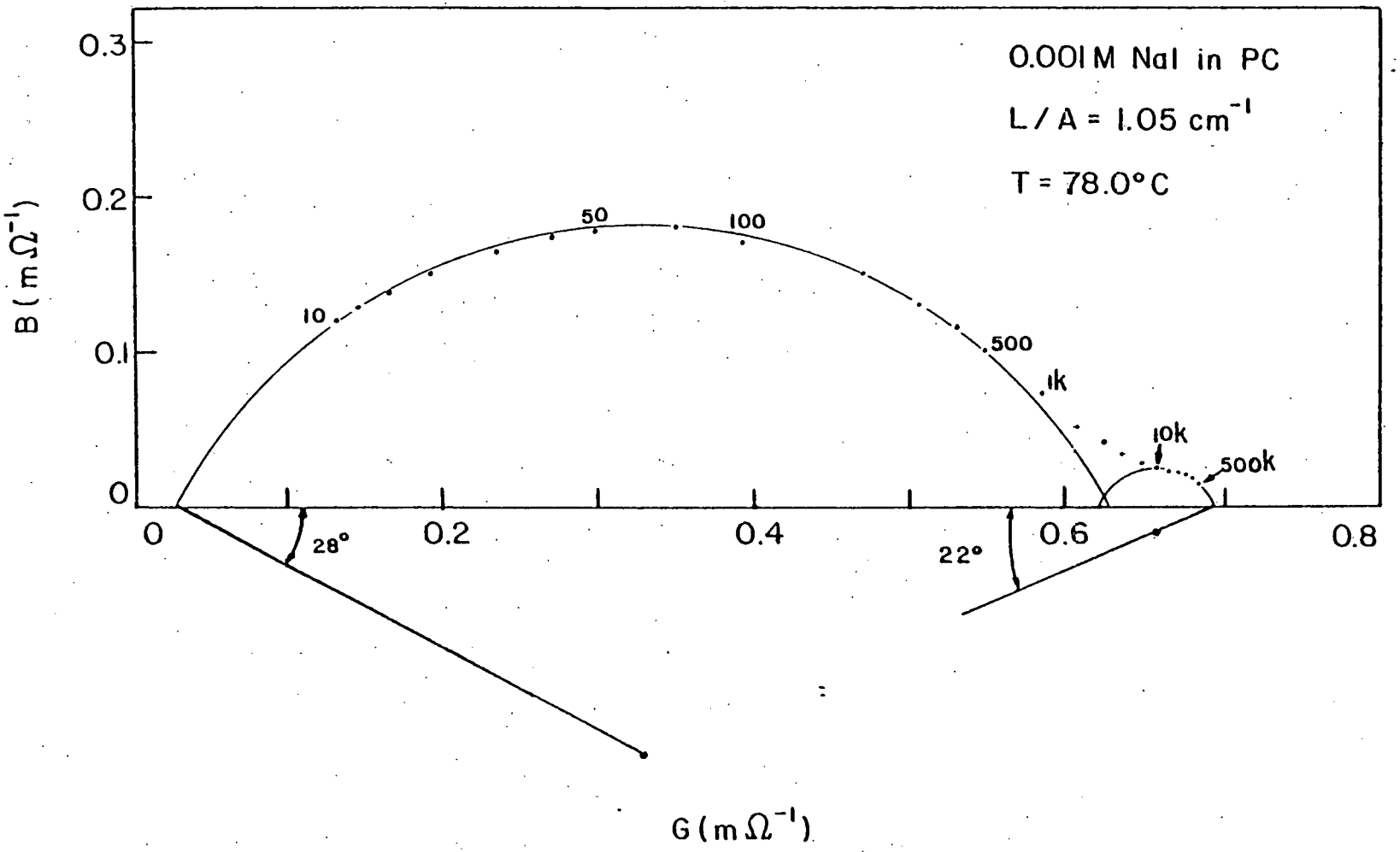
0.001 M NaI in PC
L / A = 1.05 cm⁻¹
T = 78.0°C
B (mΩ⁻¹)
G (mΩ⁻¹)
0.3
0.2
0.1
0
0.2
0.4
0.6
0.8
10
50
100
500
1k
10k
500k
28°
22°

Figure 23

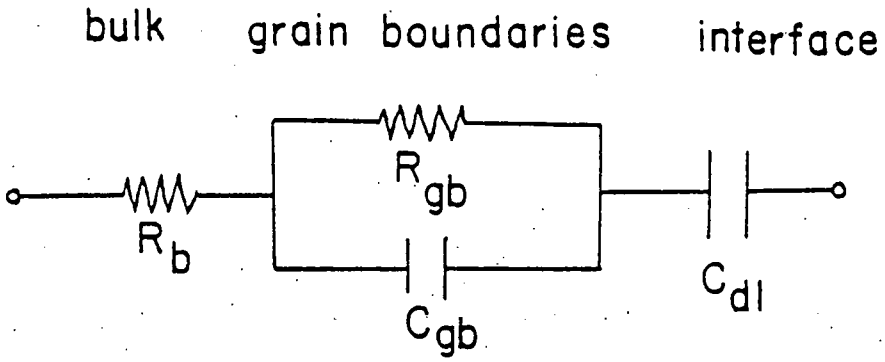
bulk
grain boundaries
interface
R_{gb}
R_b
C_{dl}
C_{gb}

(A)

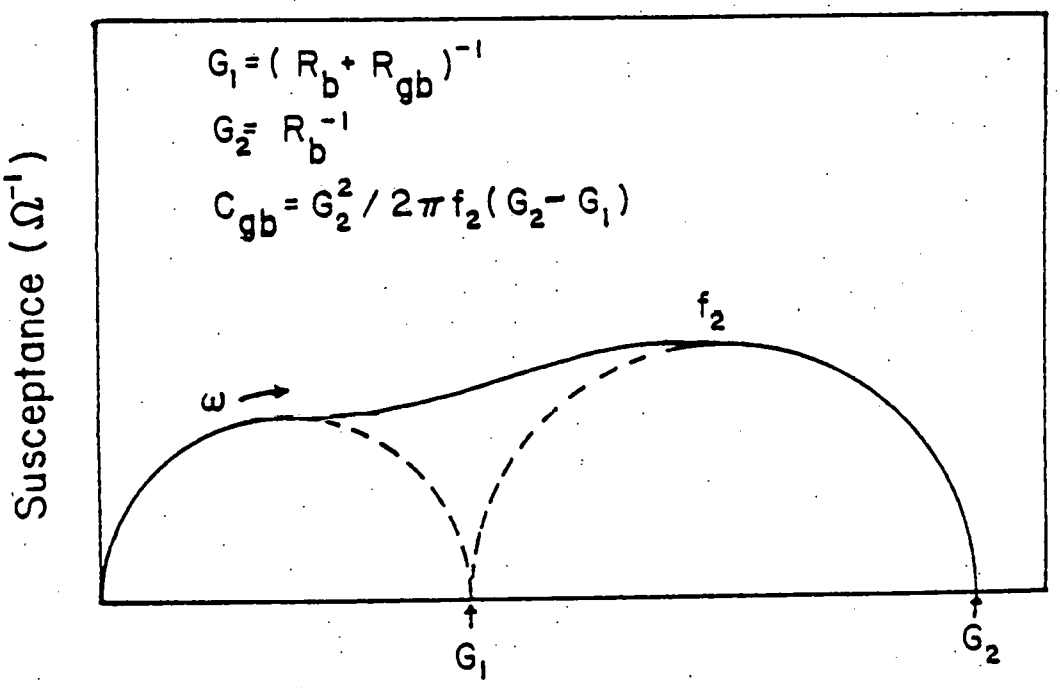
$G_1 = (R_b + R_{gb})^{-1}$
$G_2 = R_b^{-1}$
$C_{gb} = G_2^2 / 2\pi f_2 (G_2 - G_1)$
f_2
ω
G_1
G_2
Susceptance (Ω^{-1})
Conductance (Ω^{-1})

(B)

Figure 24

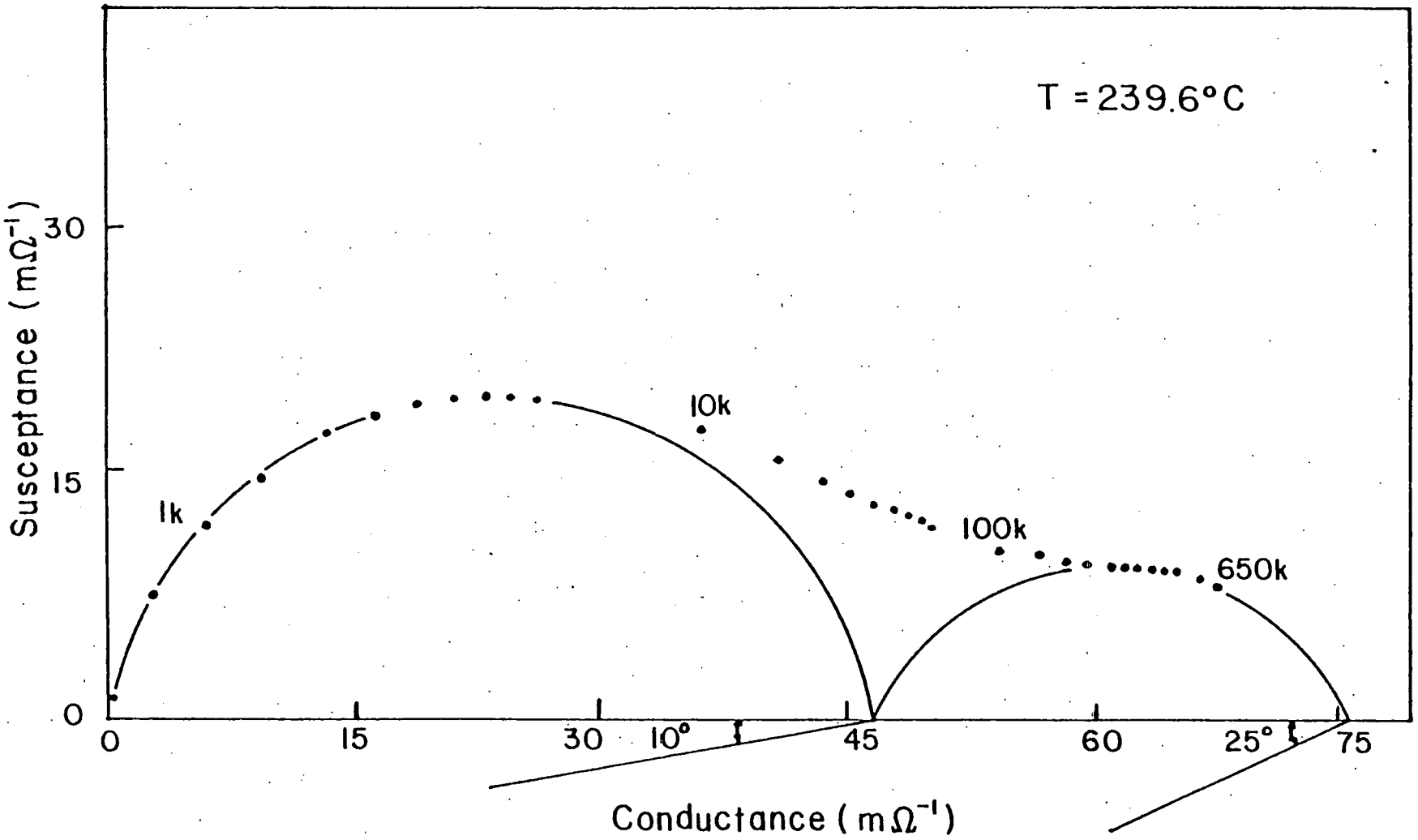
T = 239.6°C
Susceptance (mΩ⁻¹)
30
15
0
1k
10k
100k
650k
0
15
30
10°
45
60
25°
75
Conductance (mΩ⁻¹)

Figure 25

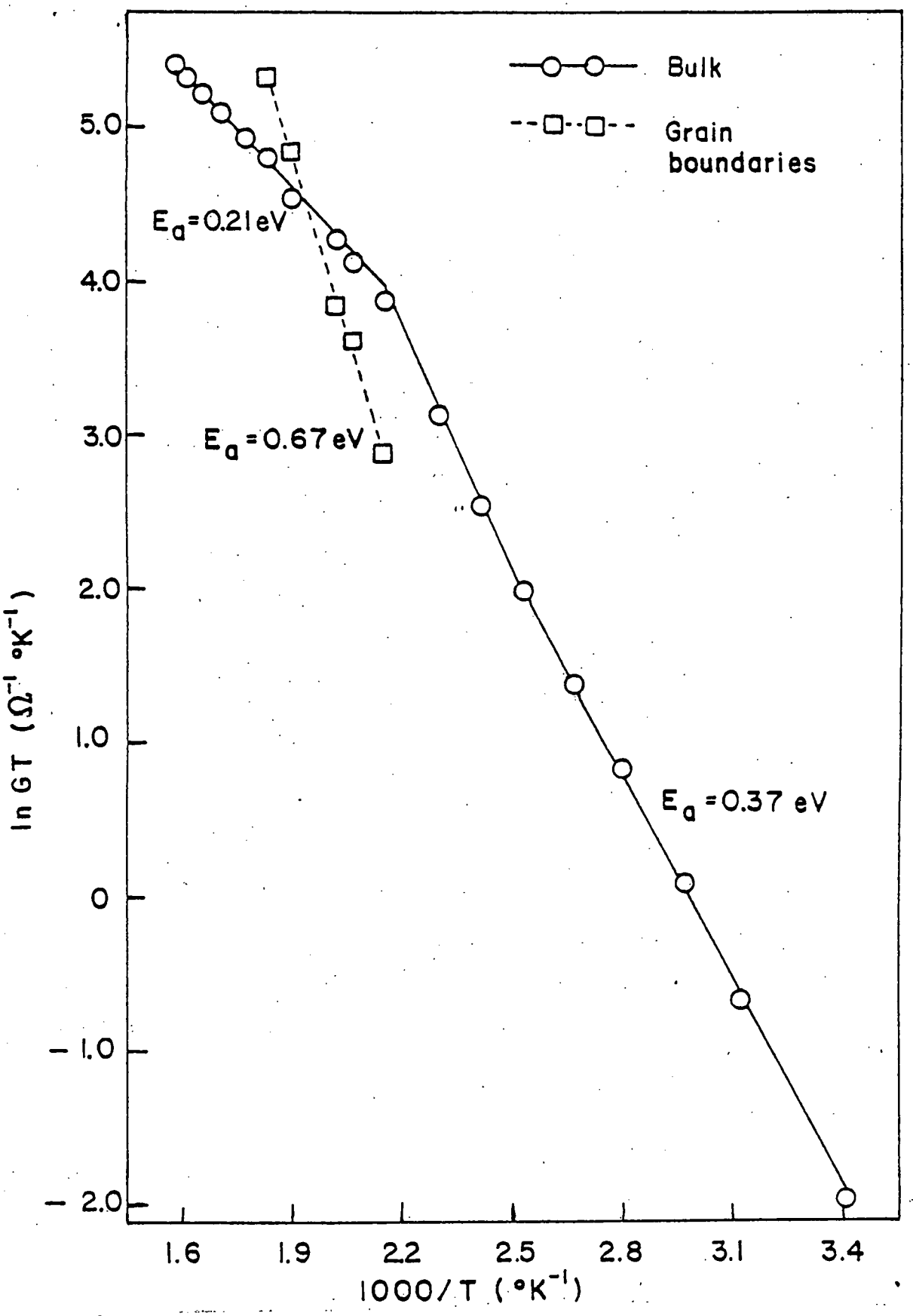
Bulk
Grain boundaries
E_a=0.21eV
E_a=0.67eV
E_a=0.37 eV
5.0
4.0
3.0
2.0
1.0
0
− 1.0
− 2.0
ln GT (Ω^{-1} °K^{-1})
1.6
1.9
2.2
2.5
2.8
3.1
3.4
1000/T (°K^{-1})

Figure 26

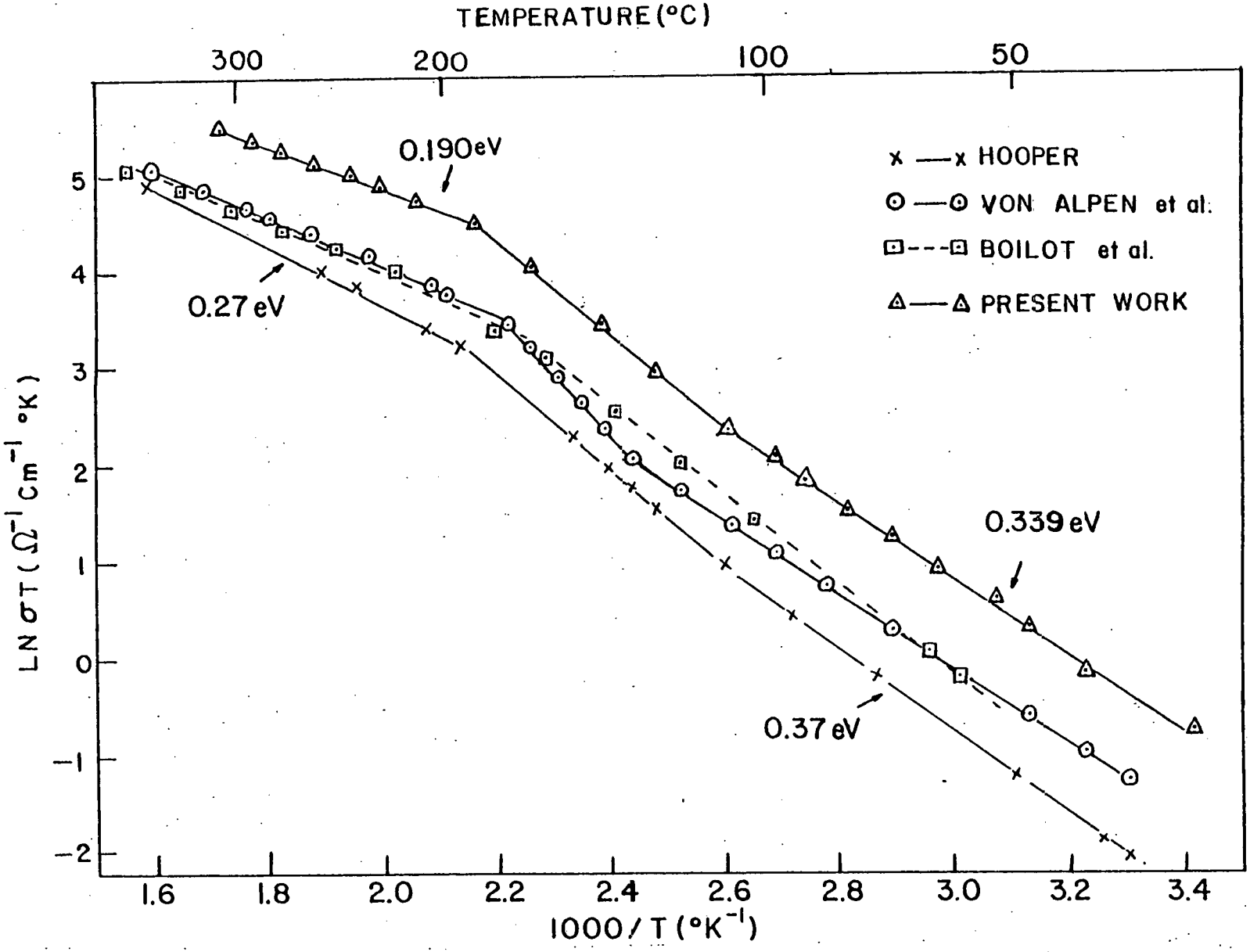
TEMPERATURE (°C)
300
200
100
50
0.190eV
0.27 eV
0.339 eV
0.37 eV
x —x HOOPER
⊙—⊙ VON ALPEN et al.
⊡---⊡ BOILOT et al.
△—△ PRESENT WORK
LN σT (Ω⁻¹ cm⁻¹ °K)
5
4
3
2
1
0
−1
−2
1.6
1.8
2.0
2.2
2.4
2.6
2.8
3.0
3.2
3.4
1000/T (°K⁻¹)

Figure 27

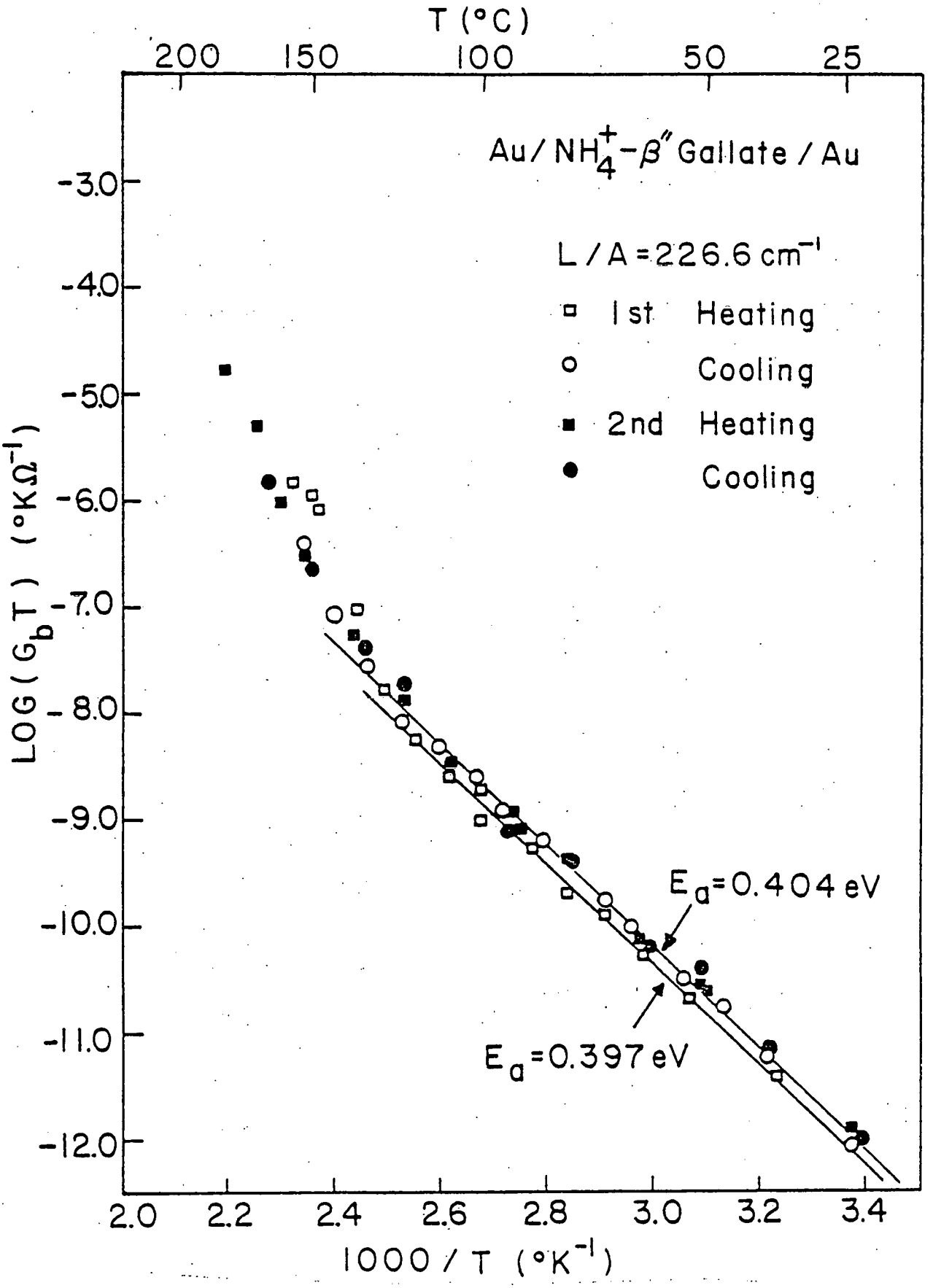
T (°C)
200
150
100
50
25
Au / NH_4^+-β″ Gallate / Au
L / A = 226.6 cm^{-1}
1st Heating
Cooling
2nd Heating
Cooling
E_a = 0.404 eV
E_a = 0.397 eV
LOG (G_b T) (°KΩ^{-1})
-3.0
-4.0
-5.0
-6.0
-7.0
-8.0
-9.0
-10.0
-11.0
-12.0
2.0
2.2
2.4
2.6
2.8
3.0
3.2
3.4
1000 / T (°K^{-1})

Figure 28

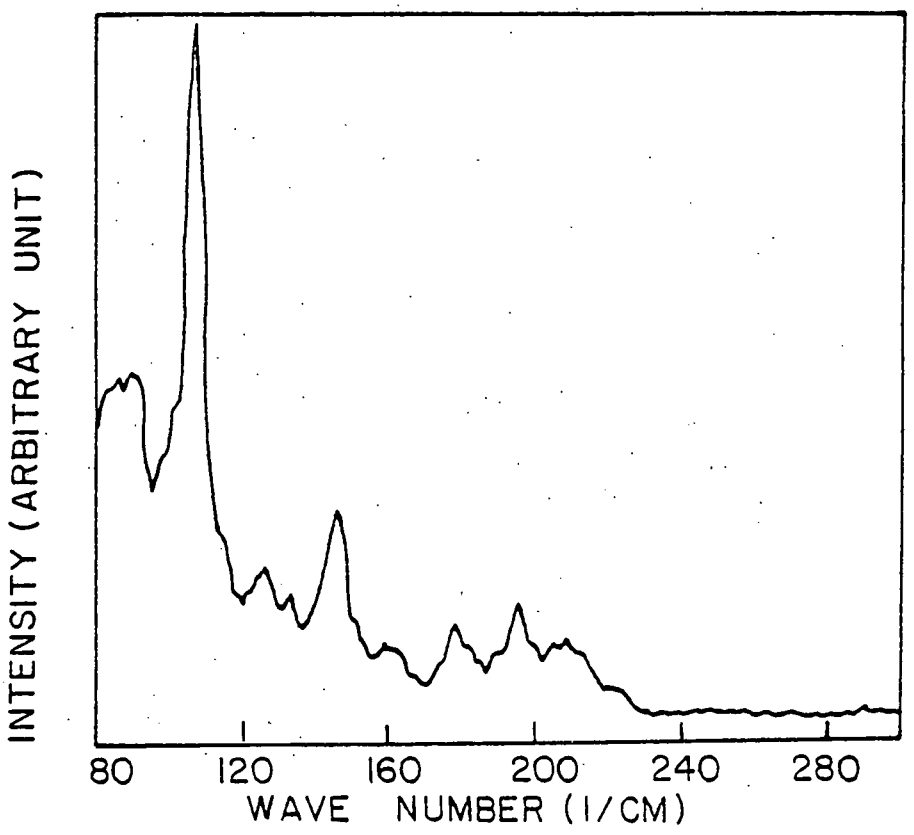
INTENSITY (ARBITRARY UNIT)
80
120
160
200
240
280
WAVE NUMBER (1/CM)

Figure 29

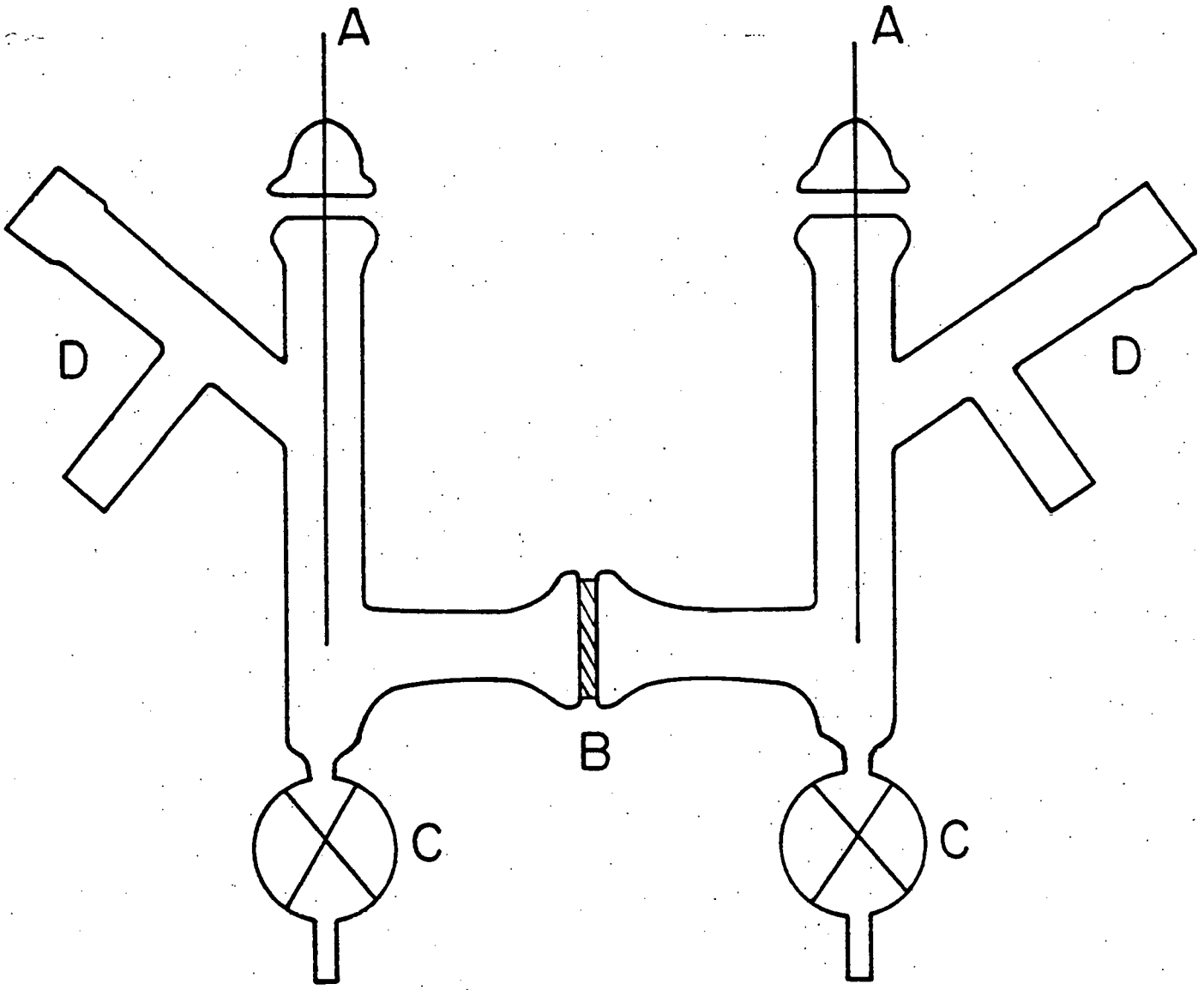

Figure 30

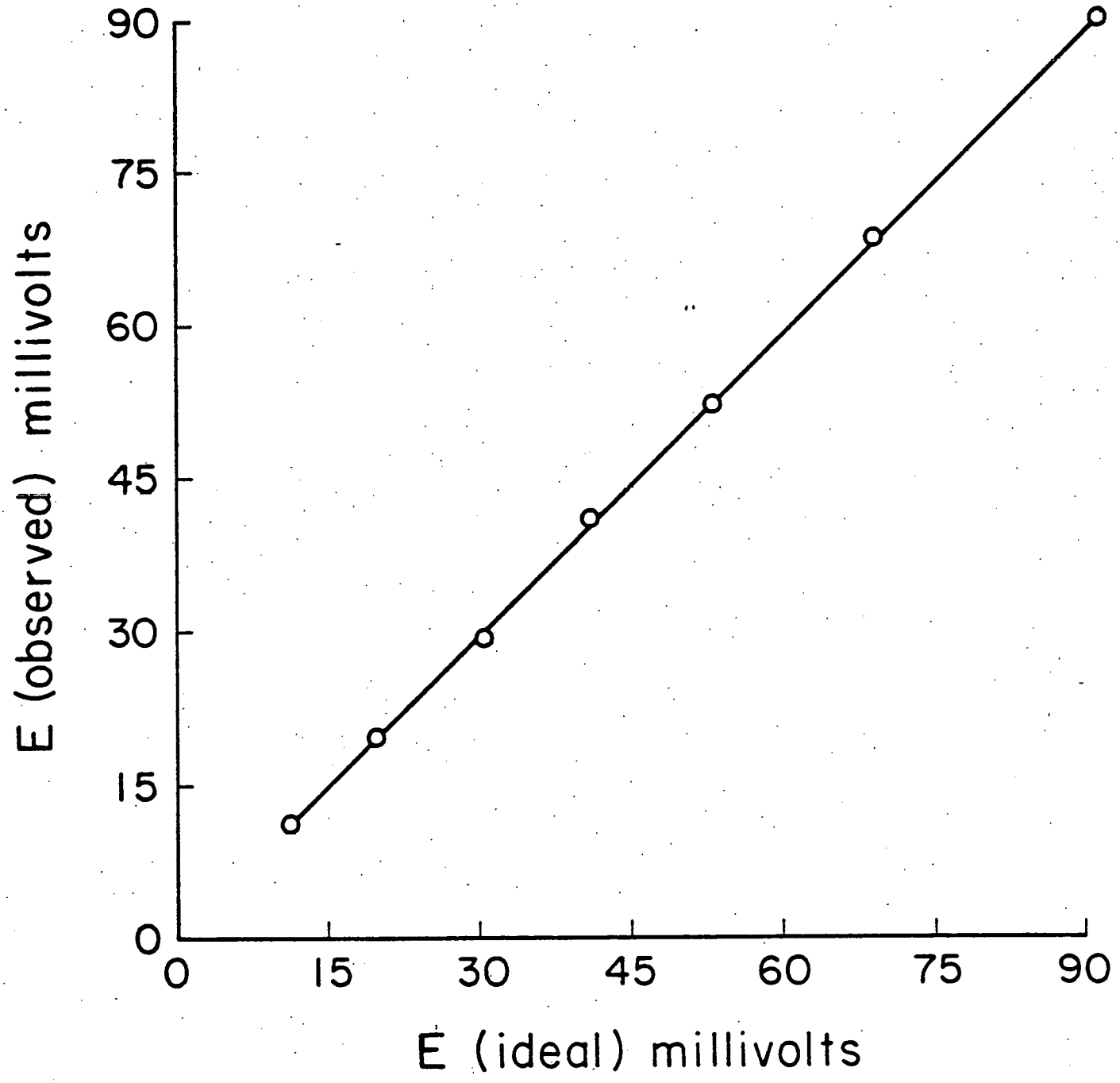
E (observed) millivolts
90
75
60
45
30
15
0
0
15
30
45
60
75
90
E (ideal) millivolts

Figure 31

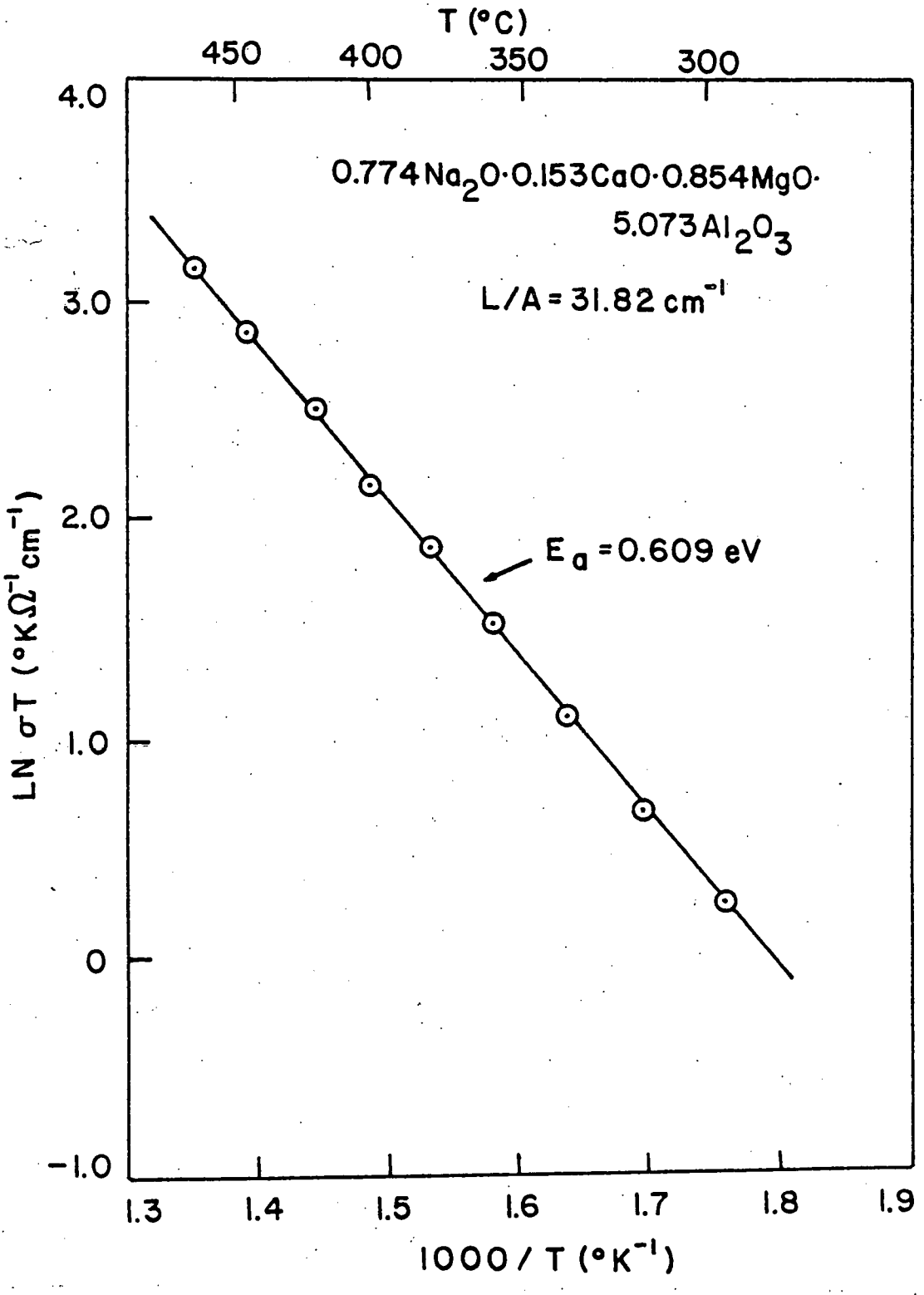
T (°C)
450
400
350
300
4.0
3.0
2.0
1.0
0
-1.0
0.774Na2O·0.153CaO·0.854MgO·
5.073Al2O3
L/A = 31.82 cm-1
Ea = 0.609 eV
LN σT (°KΩ-1cm-1)
1.3
1.4
1.5
1.6
1.7
1.8
1.9
1000 / T (°K-1)

Figure 32

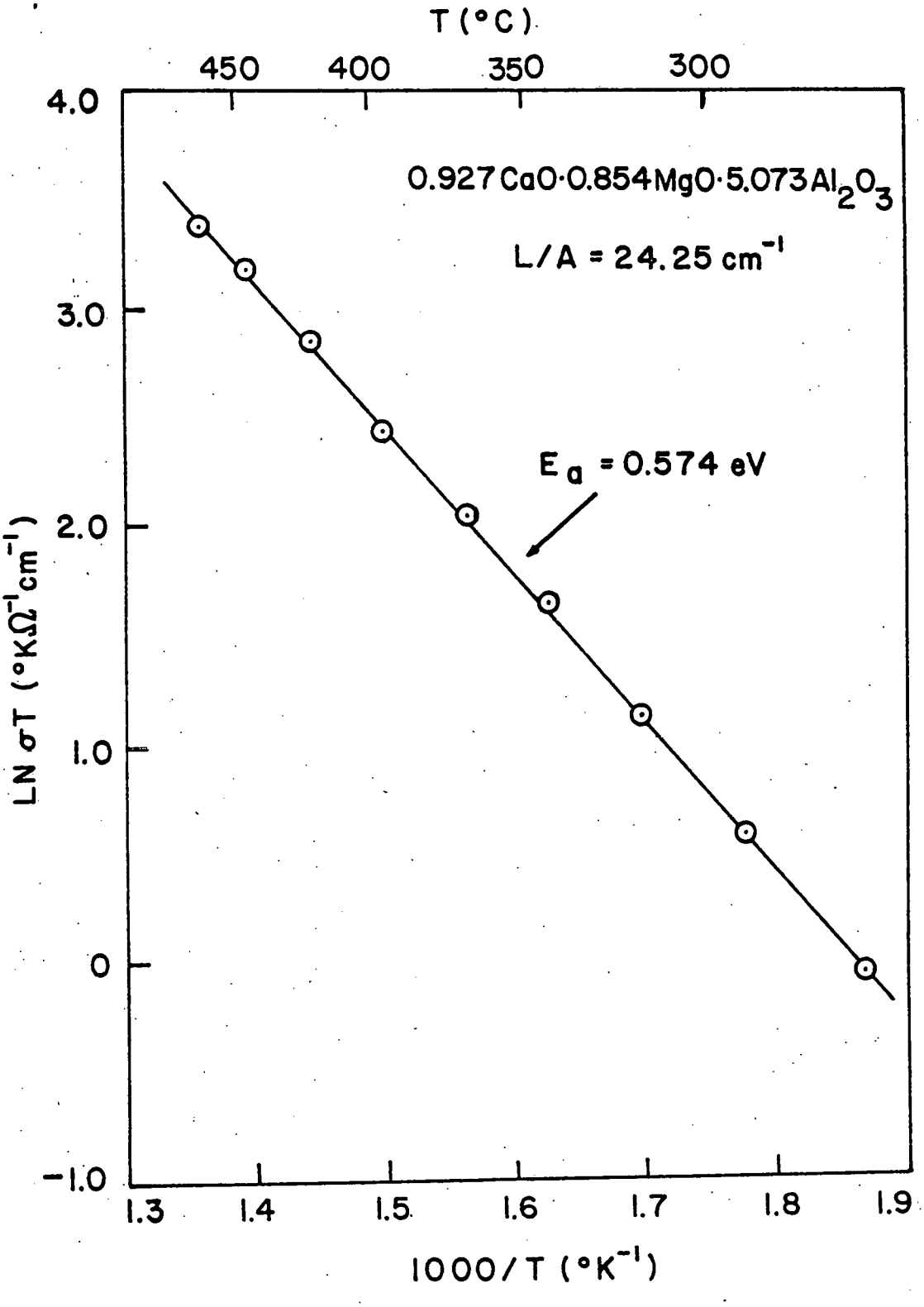
T (°C)
450
400
350
300
4.0
3.0
2.0
1.0
0
-1.0
0.927CaO·0.854MgO·5.073Al2O3
L/A = 24.25 cm-1
Ea = 0.574 eV
LN σT (°KΩ-1cm-1)
1.3
1.4
1.5
1.6
1.7
1.8
1.9
1000/T (°K-1)

Figure 33

REFERENCES

1. J. B. Phipps and D. H. Whitmore, American Ceramic Society Conference, Abstract No. 4-JII-80, Chicago, May 1980.
2. C. C. Liang, J. Electrochem. Soc. 120, 1289 (1973).
3. C. C. Liang et.al., J. Appl. Electrochem. 8, 445 (1978).
4. M. F. Yan et.al., J. Am. Ceramic Soc. 60, 120 (1977).
5. F. Bassani and R. Thomson, Phys. Rev. 102, 1264 (1956).
6. B. B. Owens et.al., Solid Electrolytes, Topics in Applied Physics 21 (1977).
7. S. Pack et.al., J. Electrochem. Soc. 127, 2177 (1980).
8. J. C. Maxwell, A Treatise on Electricity and Magnetism (1881).
9. R. Landauer, J. Appl. Phys. 23, 779 (1952).
10. G. F. Huttig and W. Steudemann, Z. Phys. Ch. 126, 105 (1927).
11. D. K. Hohnke, J. Phys. Chem. Solids 41, 777 (1980).
12. J. A. Kafalas and R. J. Cava, in Fast Ion Transport in Solids, eds. Vashishta et al., North-Holland, New York, 1979 p. 419.
13. H. Y-P. Hong, Mat. Res. Bull. 11, 173 (1976).
14. G. R. Miller, B. J. McEntire, T. D. Hadnagy, J. R. Rasmussen, and R. S. Gordon, in Fast Ion Transport in Solids, eds. Vashishta et al., North-Holland, New York, 1979 p. 83.
15. U. von Alpen, M. F. Bell, and W. Wichelhaus, Mat. Res. Bull. 14, 1317 (1979).
16. J. P. Boilot, J. P. Salanié. G. Desplanches, and D. Le Potier, ibid., p. 1469.
17. G. Desplanches, M. Rigal, and A. Wicker, Bull. Am. Ceram. Soc. 59, 546 (1980).
18. J. B. Goodenough, H. Y-P. Hong, and J. A. Kafalas, Mat. Res. Bull. 11, 203 (1976).
19. M. L. Bayard and G. G. Barna, J. Electroanal. Chem. 91, 201 (1978).
20. A. Hooper, Second International Meeting on Solid Electrolytes, St. Andrews, Scotland (1978).
21. C. E. Hayes and D. C. Ailion, in Fast Ion Transport in Solids, eds. Vashishta et al., North-Holland, New York, 1979, p. 297.
22. R. S. Gordon, G. R. Miller, B. J. McEntire, E. D. Beck, and J. R. Rasmussen, Third International Meeting on Solid Electrolytes, Tokyo, Japan, 1980, p. 242.

23. M. Kleitz and J. H. Kennedy, in Fast Ion Transport in Solids, eds. Vashishta et al., North-Holland, New York, 1979, p. 185
24. G. C. Farrington and J. L. Briant, Science 204, 1371 (1979).
25. G. C. Farrington and J. L. Briant, in Fast Ion Transport in Solids, P. Vashishta, J. N. Mundy, and G. K. Shenoy eds., North-Holland, New York, 1979, p. 395.
26. Large single crystals of sodium β″-gallate have been successfully grown by Dr. W. Bogusz in our laboratory.
27. Raman measurements were carried out on single crystals of protonic β″-gallate (1 x 1 x 0.07 mm) with the assistance of Professor D. F. Shriver and B. Papke of the Chemistry Department, Northwestern University.
28. M. Armand, J. M. Chabagno, and M. J. Duclot, Abstract 6.5, extended Abstracts, Second International Conference on Solid Electrolytes, St. Andrews, Scotland, Sept. 20-22, 1978.
29. M. Armand, J. M. Chabagno, and M. J. Duclot, in Fast Ion Transport in Solids, P. Vashishta, J. N. Mundy, and G. K. Shenoy, Editors, p. 131, North-Holland, Amsterdam (1979).
30. D. E. Fenton, J. M. Parker, and P. V. Wright, Polymer, 14, 589 (1973).
31. P. V. Wright, British Polymer J., 7, 319 (1975).
32. D. B. James, R. S. Stein, and W. J. Macknight, Bull. Am. Phys. Soc., 24, 479 (1979).
33. R. Galli, F. A. Tropeano, P. Bazzarin, and U. Mirarchi, in Fast Ion Transport in Solids, W. van Gool, Editor, p. 573, North-Holland, Amsterdam (1973).
34. D. F. Shriver, "The Manipulation of Air-Sensitive Compounds," McGraw-Hill, New York (1969).
35. T. Mussini, A. Maina, and A. Pagella, J. Chem. Thermodyn. 3, 281 (1971).